1 **A feedback mechanism mediated by myosin II-dependent apical**

2 **targeting of Rab11 vesicles reinforces apical constriction**

3

4 Wei Chen and Bing He*

5 Department of Biological Sciences, Dartmouth College, Hanover, NH, 03755, USA

6

7 * Correspondence to: bing.he@dartmouth.edu

8

9 *Summary:*

10 During tissue morphogenesis, cell shape changes resulting from cell-generated forces

11 often require active regulation of intracellular trafficking. How mechanical stimuli

12 influence intracellular trafficking and how such regulation impacts tissue mechanics

13 are not understood. We identify a mechanosensitive mechanism involving Rab11

14 recycling endosomes in regulating apical constriction in the *Drosophila* embryo.

15 During *Drosophila* mesoderm invagination, apical actin and myosin II (actomyosin)

16 contractility induces accumulation of Rab11-marked vesicles near the apical

17 membrane by promoting a directional bias in vesicle transport, which is mediated by

18 the microtubule motor dynein. At the apical domain, Rab11 vesicles are targeted to

19 the adherens junctions (AJs). The apical accumulation of Rab11 vesicles is essential

20 to prevent fragmented apical AJs, breaks in the supracellular actomyosin network and

21 a reduction in the apical constriction rate, which is separate from the function of

22 Rab11 in promoting apical myosin II activation. These findings provide evidence for a

23 mechanosensitive feedback mechanism between actomyosin-mediated apical

24 constriction and Rab11-mediated intracellular trafficking that regulates the force

25 generation machinery during tissue folding.

26

27 *Key word:*

28 Apical constriction, actomyosin contractility, Rab11, adherens junction,

29 mechanosensitive feedback

Introduction:

30

31   Cell-generated mechanical forces play a central role in tissue morphogenesis.

32   Genetically prescribed cellular forces can drive cell shape change and cell motion as a

33   direct physical outcome, thereby mediating spatially and temporally defined tissue

34   deformation (Collinet and Lecuit, 2021; Gilmour et al., 2017). In addition, mechanical

35   forces can impact morphogenesis by triggering various cellular activities ranging

36   from cytoskeleton reorganization to changes in gene expression (Fletcher and

37   Mullins, 2010; Kirby and Lammerding, 2016; Sun and Irvine, 2016; Uhler and

38   Shivashankar, 2017). Such active processes allow cells and tissues to respond to

39   mechanical inputs adaptively and thereby increase the robustness of tissue

40   morphogenesis. However, our knowledge of the active response of cells to

41   mechanical forces remains limited.

42

43   In this work, we used mesoderm invagination during *Drosophila* gastrulation as a

44   model to study how cells respond to mechanical forces generated by actomyosin

45   contractions. Immediately before gastrulation, *Drosophila* embryos undergo an

46   atypical cleavage called cellularization, during which peripherally localized syncytial

47   nuclei are partitioned into a monolayer of epithelial cells (Mazumdar and Mazumdar,

48   2002). Mesoderm invagination is initiated by actomyosin mediated apical constriction

49   in a 12-cell wide region in the ventrally localized mesodermal primordium (Leptin

50   and Grunewald, 1990; Sweeton et al., 1991). These cells subsequently invaginate as

3

51   the epithelium bends inwards, resulting in the formation of a furrow on the ventral

52   side of the embryo. The upstream signaling pathway that activates apical constriction

53   has been well characterized (reviewed in Gilmour et al., 2017; Martin, 2020; Gheisari

54   et al., 2020). In response to the dorsal-ventral patterning information, the prospective

55   mesodermal cells express two transcription factors, Twist and Snail, which in turn

56   trigger the apical recruitment and activation of RhoGEF2 through GPCR signaling.

57   RhoGEF2 further activates the small GTPase Rho1 (the *Drosophila* homologue of

58   RhoA) and leads to the activation of Rho1's effector Rho-associated protein kinase

59   (Rok). Phosphorylation of the regulatory light chain of non-muscle myosin II by Rok

60   activates myosin II at the apical cortex, where it forms an actomyosin network that is

61   physically connected to apical AJs (Amano et al., 1996; Kimura et al., 1996; Winter et

62   al., 2001; Nikolaidou and Barrett, 2004; Dawes-Hoang et al., 2005; Mason et al.,

63   2013; Vasquez et al., 2014). Within individual cells, the apical actomyosin network

64   undergoes pulsed contractions, pulling the AJ sites inwards and reducing apical cell

65   area in a ratchet-like manner (Martin et al., 2009). At a tissue level, the contractile

66   forces are integrated through AJs, resulting in progressive apical area reduction in the

67   presumptive mesoderm (Martin et al., 2010; Mason et al., 2013; Martin and

68   Goldstein, 2014).

69

70   Apical constriction can drive reorganization from subcellular to tissue levels through

71   both active and passive means. Apical constriction drives a tissue-scale viscous flow

4

72   at the tissue interior, which mediates cell shape changes across the depth of the tissue

73   (He et al., 2014). Certain organelles, such as the nucleus, appear to move passively

74   with the flow by advection (Gelbart et al., 2012). Other subcellular structures, in

75   contrast, undergo active reorganization in response to apical forces. For example,

76   apical actomyosin contractility has been shown to mediate an apical shift of the AJs at

77   the beginning of gastrulation and protects these AJs from Snail-mediated disassembly

78   (Weng and Wieschaus, 2016). More recently, apical constriction was shown to

79   promote the formation of a medioapically-localized noncentrosomal microtubule-

80   organization center that mediates microtubule reorganization during ventral furrow

81   formation (Ko et al., 2019). It remains unclear whether other subcellular structures

82   also undergo active remodeling in response to apical constriction.

83

84   Rab11, a small GTPase of the Rab family, is a well-established marker for recycling

85   endosomes (Welz et al., 2014). Like typical small GTPases, Rab11 switches between

86   active and inactive states depending on the phosphorylation state of its bound guanine

87   nucleotide. In addition to recycling endosomes, Rab11 has also been reported to

88   localize to the trans-Golgi network (TGN) and post-Golgi vesicles. It functions in

89   both exocytic and endocytic recycling pathways by regulating vesicular transport

90   from TGN and recycling endosomes to the plasma membrane (Benli et al., 1996; Jedd

91   et al., 1997; Ullrich et al., 1996; Chen et al., 1998; Pelissier et al., 2003; Takahashi et

92   al., 2012; Welz et al., 2014). At the molecular level, Rab11 regulates multiple

93   vesicular trafficking steps, including vesicle formation, transport and tethering. The

94   functions of Rab11 are mediated through its downstream effectors. For example,

95   Rab11 directly interacts with the actin motor myosin V (Lapierre et al., 2001;

96   Lipatova et al., 2008). It can also form complexes with microtubule motors dynein

97   and kinesins through a group of effector proteins called Rab11-FIPs (Rab11-family

98   interacting proteins) (Welz et al., 2014). These interactions allow Rab11 vesicles to be

99   transported along both actin and microtubule filaments (Horgan et al., 2010;

100   Schonteich et al., 2008; Schuh, 2011; Wang et al., 2008). Rab11 also interacts with the

101   Sec15 subunit of the exocyst, a protein complex critical for the tethering of secretory

102   vesicles to the plasma membrane (Mei and Guo, 2018). This interaction is important

103   for directing Rab11 vesicles to specific sites of the plasma membrane for exocytosis

104   (Zhang et al., 2004; Wu et al., 2005; Langevin et al., 2005; Oztan et al., 2007;

105   Takahashi et al., 2012).

106

107   Here, we found that apical constriction induces biased transport of Rab11-positive

108   vesicles towards the cell apex in a dynein- and microtubule-dependent manner,

109   resulting in apical accumulation of the vesicles. The bias in transport depends on

110   apical myosin II activity and quickly diminishes upon acute inactivation of apical

111   actomyosin contractility, indicating the involvement of a rapid mechanosensitive

112   response. At the apical side, Rab11 vesicles are targeted to AJs and function to

113   reinforce them during apical constriction, which in turn promotes the structural

6

114   integrity of the supracellular actomyosin network as tissue tension increases. This

115   mechanosensitive function of Rab11 is separate from its role in apical myosin II

116   activation and instead serves as a feedback regulation for apical constriction.

117   Together, our findings reveal a mechanosensitive interplay between actomyosin-

118   mediated apical constriction and Rab11-mediated vesicular trafficking that regulates

119   the actomyosin force generation machinery during epithelial folding.

120

Results:

Rab11 accumulates apically in the constricting cells during ventral furrow formation

To probe potential changes in subcellular organization in cells undergoing apical constriction, we examined a number of fluorescently tagged protein markers for different intracellular compartments during ventral furrow formation (Figure S1). Among all the markers we examined, Rab11 labeled compartments showed the most striking morphological and positional changes during apical constriction (Figure 1A, B; Movie 1). Before gastrulation started, Rab11 mainly localized to a large perinuclear compartment at the apical side of each nucleus (hereafter "perinuclear Rab11 compartment"; Figure 1C, green arrows). In addition, some vesicle-like structures were present near the basal side of the perinuclear Rab11 compartments (hereafter "Rab11 vesicles"; Figure 1C, red arrows). As the cells constricted apically, perinuclear Rab11 compartments moved basally following the basal movement of the nuclei and became moderately elongated apicobasally (Figure 1C, blue outlines). Meanwhile, Rab11 vesicles appeared near the cell apices and accumulated apically (Figure 1B-D). No apical accumulation of Rab11 vesicles occurred in the surrounding, non-constricting cells (Figure 1B-D). The Rab11 vesicles were highly dynamic, yet at any given time the majority accumulated either adjacent to or slightly basal to the apical actomyosin network (Figure 1E). We did not observe obvious apical enrichment for the other organelles we examined (Figure S1). For example, the

8

142   Golgi compartments, which also appeared as punctate structures, were depleted from

143   the apical region of the constricting cells during ventral furrow formation (Figure

144   S1A). The apical enrichment of Rab11 vesicles could not be readily explained by

145   advection by cytoplasmic flow driven by apical constriction (He et al., 2014) and

146   suggests the involvement of active regulations.

147

148   **Apical accumulation of Rab11 vesicles depends on myosin II activity**

149   The spatiotemporal correlation between the apical constriction of cells and the apical

150   accumulation of Rab11 vesicles prompted us to examine whether vesicle

151   accumulation is induced by apical constriction. To this end, we inhibited apical

152   constriction by injecting embryos with the Rok inhibitor Y-27632 (Narumiya et al.,

153   2000). Injection of Y-27632 at the end of cellularization completely prevented apical

154   myosin II activation and abolished apical Rab11 vesicle accumulation (Figure 2A).

155   Next, we adapted a previously described on-stage injection protocol (Coravos and

156   Martin, 2016) to test the effect of Y-27632 injection on Rab11 vesicles after they

157   accumulated apically. After drug injection, myosin II immediately (< 1 min)

158   dissociated from the apical cortex, which was associated with a relaxation of the

159   furrow (Figure 2B') and a moderate reduction of apical Rab11 vesicles (Figure 2B).

160   About 4 minutes after injection, Rab11 vesicles were largely depleted from the apical

161   surface (Figure 2B). The morphology of perinuclear Rab11 compartments were not

162   obviously affected by Y-27632 injection (Figure 2B, 3 – 6 μm), indicating that the

9

163   drug did not cause a general disruption of the Rab11 positive membrane structures.

164   These observations indicate that the induction and maintenance of apical

165   accumulation of Rab11 vesicles depends on apical myosin II activity.

166

167   To further test the relationship between apical myosin II activation and apical

168   accumulation of Rab11 vesicles, we examined embryos in which the myosin heavy

169   chain Zipper was depleted by RNA interference-mediated maternal knockdown.

170   Consistent with the Y-27632 treatment, Zipper knockdown also inhibited apical

171   Rab11 vesicle accumulation (Figure 2C). Conversely, we asked whether ectopic

172   activation of myosin II would induce apical accumulation of Rab11 vesicles. For this

173   purpose, we examined the mutant embryos for *Spn27A*. *Spn27A* encodes a serine

174   protease inhibitor that regulates dorsal-ventral patterning in early embryos by

175   inhibiting the Toll-Dorsal pathway (Ligoxygakis et al., 2003). Consistent with

176   previous reports, *Spn27A* mutant embryos showed a ventralized phenotype with

177   expanded apical myosin II activation domain during gastrulation (Figure 2D;

178   Ligoxygakis et al., 2003). In these embryos, Rab11 vesicles were also enriched

179   apically in cells with ectopic activation of apical myosin II (Figure 2D, D'). Taken

180   together, we conclude that apical actomyosin contractility is both necessary and

181   sufficient to induce apical accumulation of Rab11 vesicles.

182

183   **Apical Rab11 vesicles are not derived from endocytosis**

10

184   We next examined how Rab11 vesicles accumulate at the apical surface during apical

185   constriction. Rab11 vesicles may be derived from endocytosis of apical membranes.

186   Apical endocytosis has been shown to play an important role in apical constriction as

187   the apical membrane area decreases over time (Lee and Harland, 2010; Mateus et al.,

188   2011; Miao et al., 2019). To test this possibility, we blocked endocytosis by using a

189   temperature sensitive mutant of *shibire* (*shi^{ts}*), the *Drosophila* homolog of dynamin

190   (van der Bliek and Meyerowrtz, 1991). At the restrictive temperature of 32°C, *shi^{ts}*

191   mutant embryos exhibited ventral furrow defects with different levels of severity,

192   ranging from slower apical constriction (mild group, N = 10 embryos) to failure in

193   invagination (severe group, N = 7 embryos) (Figure S2A). Embryos in the mild group

194   showed comparable apical Rab11 vesicle accumulation to the wildtype controls

195   (Figure S2B). Embryos in the severe group showed a modest accumulation of apical

196   Rab11 vesicles before gastrulation, which was distinct from the wild type and

197   suggests the presence of early defect due to a strong loss of dynamin function.

198   Nevertheless, when gastrulation started, the amount of apical Rab11 vesicles further

199   increased in the constricting cells, resulting in more apical vesicles than the wildtype

200   controls (Figure S2B). These results indicate that endocytosed apical membrane is not

201   the major source of apical Rab11 vesicles.

202

203   **Apical constriction induces apically biased transport of Rab11 vesicles**

204   An alternative possibility is that the apical Rab11 vesicles are supplied from the more

205   basal side of the cell by directional transport. To capture the rapid movement of

206   Rab11 vesicles in the apical-basal direction, we focused on the constricting cells

207   located near the medial-lateral boundaries of the constricting domain. These cells are

208   tilted towards the ventral midline at the late stage of apical constriction, making it

209   possible to follow the apical-basal movement of Rab11 vesicles by fast imaging of a

210   single focal plane (Figure 3A). Using this approach, we observed constant transport of

211   Rab11 vesicles in the axial direction in the constricting cells (Figure 3B; Movie 2).

212   There were both apically and basally directed movements, with a bias towards the

213   apical direction. Vesicle tracking revealed that the apically directed movement

214   accounted for approximately three quarters of the total transport events (74.5% $\pm$

215   5.7%; n = 255 trajectories from 3 embryos, Figure 3C-E). Other than the bias in the

216   directionality, there was no significant difference in other aspects of the trajectories

217   between apical and basal transport, including the average velocity, the duration and

218   the travel distance of the tractable trajectories (Figure 3F). These results suggest that

219   the apical bias in the direction of Rab11 vesicle transport results in the apical

220   enrichment of these vesicles.

221

222   Because the apical enrichment of Rab11 vesicles depends on apical constriction, we

223   hypothesized that the biased basal-to-apical transport of Rab11 vesicles also depends

224   on apical actomyosin contractility. To test this hypothesis, we used an optogenetic tool

225   we recently developed to acutely inhibit myosin II activity through light-sensitive

226   recruitment of a dominant negative form of Rho1 (Rho1DN) to the plasma membrane

227   ("Opto-Rho1DN", Guo et al. in preparation). The approach is based on the CIBN-

228   CRY2 system (Kennedy et al., 2010; Guglielmi et al., 2015). Blue-light dependent

229   recruitment of a CRY2-Rho1DN fusion protein to plasma membrane-anchored CIBN

230   blocks activation of endogenous Rho1, causing rapid inactivation of myosin II (Figure

231   3G, H). Using the same imaging configuration as shown in Figure 3A, we examined

232   the immediate impact of myosin II inhibition on the transport of Rab11 vesicles. As

233   expected, blue light stimulation resulted in rapid loss of apical myosin II (within ~30

234   seconds; Figure 3I). The loss of apical myosin II at this stage of ventral furrow

235   formation did not cause furrow relaxation or any obvious changes in cell orientation.

236   Strikingly, blue light stimulation resulted in a rapid change in the transport of Rab11

237   vesicles. Within the first 23 seconds after stimulation, the proportion of apical

238   transport was 62.5% (62.5% ± 5.0%; n = 257 trajectories from 3 embryos), lower than

239   that in the wildtype controls (Figure 3J). This proportion dropped to close to 50%

240   (52.3% ± 1.6%; n = 280 trajectories from 3 embryos) in the next 23-second time

241   window, indicating that the directional bias was completely abolished (Figure 3J;

242   Movie 3). There was no significant difference between the two time windows

243   regarding other aspects of transport (Figure 3K). Therefore, the main effect of myosin

244   II inhibition on Rab11 vesicle transport is to eliminate the apical bias of the transport.

245   The strong dependence of the biased transport on apical myosin II activity suggests

246   that the alteration in directionality of Rab11 vesicle trafficking is a rapid

13

247   mechanosensitive response to apical actomyosin contractility.

248

249   **The transport of Rab11 vesicles also depends on microtubules and dynein**

250   Because the saltatory and directional movement of Rab11 vesicles was reminiscent of

251   microtubule-dependent transport, we examined the spatial relationship between

252   Rab11 vesicles and microtubules by two-color imaging with mCherry-Rab11 and the

253   microtubule marker Jupiter-GFP (Karpova et al., 2006). In constricting cells,

254   abundant apical-basally oriented microtubules were present between the cell apex and

255   the nucleus. As Rab11 vesicles moved apically or basally, most of them persistently

256   associated with microtubule fibers, which represented either individual microtubules

257   or microtubule bundles (Figure 4A; Movie 4, before injection).

258

259   To further test whether the transport of Rab11 vesicles requires microtubules, we

260   performed on-stage colchicine injection during apical constriction. In less than a

261   minute after injection, most microtubules disappeared or became greatly shortened.

262   Meanwhile, the number of directional transport events significantly decreased. The

263   small number of remaining transport-like events occurred only in regions where some

264   residual microtubules remained, which provided further evidence that the transport of

265   Rab11 vesicles in normal cells is microtubule dependent (Figure 4B; Movie 4).

266

267   To further test our hypothesis, we examined the impact of colchicine injection on the

14

268   apical accumulation of Rab11 vesicles. Injection of embryos at late cellularization (N

269   = 5 embryos) resulted in a significant reduction in the apical accumulation of Rab11

270   vesicles compared to control embryos (N = 4 embryos) (Figure 4C-F). Importantly,

271   the activation of apical myosin II was normal in these embryos, which is consistent

272   with a recent report (Ko et al., 2019). Therefore, the impact of microtubule disruption

273   on Rab11 vesicle accumulation is not due to an indirect effect of disrupting apical

274   myosin II activation. These results support our hypothesis that the biased transport of

275   Rab11 vesicles along microtubules leads to their apical accumulation.

276

277   Unexpectedly, injection of colchicine at or after the onset of gastrulation (N = 5

278   embryos) resulted in a wider range of phenotypes, and on average there was no

279   significant reduction of vesicle numbers compared to the control embryos (Figure 4C-

280   F). We speculate that disruption of microtubules after the onset of gastrulation not

281   only reduces the apical-basal transport of Rab11 vesicles but also inhibits the turnover

282   of the vesicles that are already accumulated apically. This combined effect may

283   obscure the net effect of loss of microtubules.

284

285   Next, we sought to test the role of microtubule motors on the transport of Rab11

286   vesicles. We found that injection of antibody against the dynein intermediate chain

287   (DIC) (Yi et al., 2011) during apical constriction resulted in a rapid reduction of

288   vesicle transport events in both directions, whereas injection of a control GST

289   antibody had no effect (Figure 4G, Movie 5). Furthermore, the apical accumulation of

290   Rab11 vesicles was greatly reduced in dynein antibody-injected embryos but not in

291   the control antibody-injected embryos (Figure 4H). Whereas we were not able to test

292   the role of kinesin motors due to a lack of functional reagents, the pronounced impact

293   of dynein inhibition on Rab11 vesicle transport and accumulation suggests that dynein

294   plays a predominant role in the apical-basal transport of Rab11 vesicles during apical

295   constriction. When apical constriction starts, the centrosomes in the constricting cells

296   move basally together with the nuclei (Ko et al., 2019). Microtubules originating from

297   these centrosomes are expected to have their plus ends pointing toward the apical

298   side. Meanwhile, the microtubule minus end binding protein Patronin is enriched at

299   the medio-apical cortex (Ko et al., 2019), where it organizes a microtubule population

300   with their minus ends pointing to the apical side. Our observation that inhibiting

301   dynein abolishes both apical and basal transport of Rab11 vesicles may reflect the

302   bidirectional nature of the microtubule populations.

303

304   **Rab11 reinforces apical AJs during apical constriction**

305   We next sought to determine the function of apically accumulated Rab11 vesicles.

306   Single plane fast imaging analysis revealed that Rab11 vesicles remained very

307   dynamic after they arrived at the cell apices, with a substantial fraction delivered to

308   apical AJs (Figure 5A; Movie 6). The enrichment of Rab11 vesicles at AJs was

309   particularly obvious during the early stage of apical constriction when apical AJs had

310   not yet formed a continuous belt and instead were observed as discrete foci. Intensity

311   profiling of Rab11 and E-cadherin along the apical cell-cell boundaries in constricting

312   cells revealed a positive correlation. In contrast, the intensity profiles of Rab11 and a

313   general membrane marker P4M, a PI(4)P binding protein, showed no significant

314   correlation (Figure 5B-D). It remains unclear whether the targeting of Rab11 vesicles

315   to the cell periphery is followed by fusion of vesicles with the plasma membrane, as

316   demonstrated in some other systems (Grünfelder et al., 2003; Takahashi et al., 2012).

317   We were not able to detect an obvious plasma membrane-associated signal for Rab11.

318   One possibility is that Rab11 is only transiently associated with the plasma membrane

319   due to GTP hydrolysis. Consistent with this view, a constitutively active form of

320   Rab11 (Rab11CA), which is locked in its GTP-bound state, showed a strong cell

321   membrane localization in addition to the vesicle form, and the cell membrane signal

322   was enhanced when the cells constricted apically (Figure S3).

323

324   The enrichment of Rab11 vesicles near the apical AJs prompted us to propose that

325   Rab11 vesicles regulate the structure and function of AJs. To test this hypothesis, we

326   inhibited Rab11 activity by injecting embryos with a purified dominant negative

327   Rab11 mutant (Rab11DN), which blocks the activation of endogenous Rab11 by

328   binding to and sequestering the guanine nucleotide exchange factors (GEFs) for

329   Rab11 (Ullrich et al., 1996). Importantly, the injection approach allows stage-specific

330   inhibition of Rab11, which is critical for bypassing the requirement for Rab11 in pre-

17

331   gastrulation stages (Pelissier et al., 2003; Riggs et al., 2003; Tiwari and Roy, 2008).

332   Injection of Rab11DN at mid/late cellularization completely prevented the

333   accumulation of apical Rab11 vesicles during apical constriction (N = 5/5); whereas

334   injection of Rab11DN close to the onset of apical constriction either eliminated

335   apically accumulated Rab11 vesicles (in 4.35 ± 1.31 min, N = 24/31; Figure 5E;

336   Movie 7) or decreased their number (N = 7/31). In contrast to Rab11 vesicles, the size

337   and morphology of perinuclear Rab11 compartments were not immediately affected

338   by injection (Figure 5E, green arrows). These results suggest that both the initiation

339   and maintenance of the apical accumulation of Rab11 vesicles require active Rab11.

340

341   To determine whether the apical accumulation of Rab11 vesicles is important for the

342   formation or maintenance of AJs, we examined the effects of Rab11DN injection on

343   E-cadherin-GFP. In control GST-injected embryos, apical AJs became more

344   continuous and belt-like as apical constriction progressed (Figure 5F). In contrast,

345   Rab11DN- injected embryos showed fragmented junctions at comparable stages

346   (Figure 5F). Furthermore, the junctional component Jub, an Ajuba LIM protein that

347   localizes to the AJs (Razzell et al., 2018), was greatly depleted from AJs upon

348   Rab11DN injection (Figure 5G). In addition to the junctional defects, the cell area

349   within the constriction domain became more heterogeneous after Rab11DN injection,

350   raising the possibility that defects in AJ organization disrupt apical constriction

351   (Figure 5F; see below). Together, these results suggest a role for apical Rab11 vesicles

18

352   in reinforcing apical AJs. Such a mechanosensitive reinforcement of AJs might be

353   important for maintaining tissue integrity as tension increases in the constriction

354   domain due to contractions of the actomyosin network.

355

356   **Rab11 regulates myosin II organization and promotes apical constriction**

357   Given the important role of apical AJs in the spatial organization of the supracellular

358   actomyosin network (Martin et al., 2010; Sawyer et al., 2009), we examined whether

359   inhibition of Rab11 activity would cause defects in apical constriction. Injection of

360   Rab11DN at mid/late cellularization (< 20 min before gastrulation) resulted in an

361   overall slower rate of apical constriction compared to GST injected embryos (Figure

362   S4A, B). The difference between control and Rab11DN injection groups was

363   relatively small in the first ~ 5 minutes after the onset of gastrulation but became

364   much more prominent after 5 minutes (Figure S4B). In the control group, the average

365   cell area continued to decrease from 2 min to 8 min. In contrast, in Rab11DN

366   injection group, whereas the average cell area noticeably decreased from 2 min to 5

367   min, the area reduction was greatly attenuated from 5 min to 8 min (Figure S4C-D).

368   As a result, the average apical area in the Rab11DN injection group became

369   substantially larger than that in the control group at 8 min despite the similarity

370   between the two groups at 2 min (Figure S4E). These results suggest that the apical

371   accumulation of Rab11 vesicles is important for preventing apical constriction defect

372   at late stages of apical constriction.

19

373

374   To investigate the cause of the apical constriction defect, we examined the dynamics

375   and organization of apical myosin II in embryos injected with Rab11DN around the

376   onset of gastrulation. Despite the prompt elimination of Rab11 vesicles, Rab11DN

377   injection did not cause any obvious defect in the apical activation of myosin II. The

378   width of the tissue that showed apical myosin II accumulation, as well as the average

379   intensity of apical myosin II during apical constriction, were comparable between

380   control and Rab11DN injected groups (Figure 6A-C, GST vs. Rab11DN late

381   injection; Movie 8). However, quantification of the rate of myosin flow towards the

382   ventral midline at approximately 6 – 7 minutes into gastrulation showed a

383   significantly lower rate of apical constriction in Rab11DN injected embryos compared

384   to control embryos (Figure 6D-G), which was consistent with the results obtained by

385   analyzing cell membrane markers (Figure S4A-E). Interestingly, the apical

386   constriction defect in Rab11DN injected embryos was associated with frequent breaks

387   within the apical actomyosin network, which was rarely seen in the control embryos

388   (Figure 6H, J; Movie 9). These myosin breaks occurred randomly across the

389   constriction domain and were usually promptly reconnected, which prevented the

390   complete tearing apart of the network. The higher frequency of myosin breaks, even

391   though transient, can slow down apical constriction and cause temporary force

392   imbalances between neighboring cells that increase heterogeneity in the apical cell

393   area (Figure 5F).

394

395   The lack of defects in apical myosin activation upon Rab11 inhibition apparently

396   contradicted with previous findings that Rab11 is required for apical myosin

397   activation in several other apical constriction-mediated tissue folding processes

398   (Ossipova et al., 2014, 2015; Le and Chung, 2021). In these studies, Rab11 was

399   typically inhibited at a stage much earlier than the onset of apical constriction. We

400   therefore tested whether Rab11 also has an earlier function that is required for apical

401   myosin II activation during ventral furrow formation. We found that injection of

402   Rab11DN proteins during early cellularization (> 30min before the onset of

403   gastrulation) indeed resulted in a strong reduction or lack of apical myosin

404   accumulation during gastrulation (Figure 6A, B). Therefore, through injection

405   mediated acute inhibition of Rab11, we were able to resolve the early and late

406   functions of Rab11 in apical constriction and identify a previously unappreciated,

407   mechanosensitive function of Rab11 in regulating the spatial organization of the

408   actomyosin network after myosin II activation.

409

410   We then investigated what caused myosin breaks in Rab11DN injected embryos. We

411   noticed that AJs were often pulled to the opposite side from where myosin breaks

412   happened, indicating the decoupling of actomyosin network and AJs from one side of

413   the cell-cell boundary (Figure 6I, red arrows). This observation suggests that the

414   increased frequency of myosin breaks is due to impaired connections between

21

415   junction and the actomyosin network as a consequence of altered junction

416   organization. Supporting this view, we observed similar myosin breaks in embryos

417   defective in *canoe*, the *Drosophila* Afadin homolog that regulates the linkage of the

418   actin cytoskeleton to AJs during apical constriction (Movie 10). We hypothesized that

419   the consequences of weakening AJ-actomyosin connections would likely become

420   more prominent during later phases of apical constriction when the tissue tension

421   becomes high. In line with this prediction, myosin breaks in the Rab11DN-injected

422   embryos became prominent only during later phases of apical constriction (Movie 8),

423   which resulted in a stage-specific defect in apical constriction (Figure S4C-D).

424

425   In addition to myosin breaks, we observed a second phenotype in the spatial

426   organization of apical myosin II. Instead of forming a supracellular meshwork with

427   medioapically enriched myosin foci connected by myosin fibers, myosin II instead

428   formed ring-like circular structure at the apical domain of each constricting cell

429   (Figure 6A). These apical myosin rings appeared to be connected with each other,

430   suggesting that actomyosin contractions could remain integrated across the

431   mesodermal tissue. Interestingly, a recent study showed that loss of anisotropy in

432   apical tension led to similar myosin ring formation in the constricting cells (Chanet et

433   al., 2017). In Rab11DN-injected embryos, most myosin breaks occurred in the

434   anterior-posterior (AP) orientation (Figure 6K), which is the direction in which

435   tension is higher (Martin et al., 2010). These breaks may dissipate tension in the AP

22

436   direction, thereby reducing tension anisotropy of the actomyosin network and causing

437   myosin ring formation. In support of this view, the constricting cells exhibited no

438   obvious increase of anisotropy in their apical geometry at the late stages of apical

439   constriction in Rab11DN injected embryos (from 5 min to 8 min). This was in sharp

440   contrast to control embryos in which anisotropy continued to increase during apical

441   constriction (Figure S4F). Together, these findings indicate that apical constriction

442   induced apical targeting of Rab11 vesicles is essential for proper spatial organization

443   and structural integrity of the supracellular actomyosin network, a function distinct

444   from Rab11's function in promoting apical myosin II activation. This

445   mechanochemical feedback mechanism allows the tissue to respond and adapt to

446   altered mechanical environment during apical constriction and maintain the integrity

447   of the force generation machinery during tissue folding.

Discussion:

448

449   Our work identifies a Rab11-dependent mechanosensitive feedback mechanism that

450   promotes proper spatial organization of apical actomyosin network during apical

451   constriction. Using a combination of genetic, optogenetic and pharmacological

452   approaches, we present evidence that during ventral furrow formation, apical

453   constriction induces dynein- and microtubule-dependent, biased transport of Rab11

454   vesicles towards the cell apices and results in enrichment of these vesicles at the

455   apical AJs. The bias in transport depends on apical actomyosin contractility and is

456   rapidly diminished upon acute myosin II inactivation. Acute elimination of apical

457   Rab11 vesicles through Rab11DN injection resulted in fragmented apical AJs, which

458   impaired the integrity of the apical supracellular actomyosin network as tension builds

459   up in the network. Together, our findings suggest that the mechanosensitive regulation

460   of Rab11-mediated vesicular trafficking provides a mechanism to allow the tissue to

461   promptly adapt to rapid increases in tissue tension and maintain the integrity of the

462   force generation machinery during tissue deformation (Fig. 7).

463

464   In recent years, it has been increasingly appreciated that mechanical forces can impact

465   the process of intracellular membrane trafficking. For example, increased membrane

466   tension can suppress the formation of endocytic vesicles (Wu et al., 2017) and

467   conversely promote vesicle fusion with the lipid bilayer (Shillcock and Lipowsky,

468   2005; Staykova et al., 2011). Mechanical force-induced stimulation of exocytosis has

24

469 been observed in various contexts, including cells undergoing spreading, being

470 stretched or experiencing shear stress (Boycott et al., 2013; Gauthier et al., 2011;

471 Khandelwal et al., 2013). The impact of mechanical force on vesicle transport and

472 vesicle accumulation has also been observed. For example, mechanical tension can

473 promote synaptic vesicle accumulation at the presynaptic terminals in *Drosophila*

474 neuromuscular synapses and modulate the transport of large dense core vesicles in

475 cultured *Aplysia* neurons (Siechen et al., 2009; Ahmed et al., 2012; Ahmed and Saif,

476 2014). Our work demonstrates that vesicle transport can also be regulated by

477 endogenous contractile forces in embryonic epithelium to facilitate morphogenesis.

478 The striking observation that the directionality of Rab11 vesicle transport can be

479 modulated nearly instantaneously upon acute alteration of apical actomyosin

480 contractility demonstrates that mechanical regulation of vesicle transport can take

481 effect very rapidly and suggests the involvement of a fast mechanotransduction

482 mechanism.

483

484 How does apical constriction affect vesicle transport inside of the cell? The

485 directional bias of Rab11 vesicle transport could arise from the orientation of the

486 cytoskeletal tracks. However, we do not favor this possibility considering the bias of

487 vesicle transport diminished within one minute upon inhibition of myosin II activity,

488 which is too short for significant changes in overall microtubule polarity to happen.

489 Alternatively, apical constriction may cause changes in the activity of the motor

25

490   complexes that drive the motion of Rab11 vesicles. Our data indicate that the apically

491   biased transport of Rab11 vesicles is predominantly mediated by dynein. Regulation

492   of dynein-mediated transport can occur at multiple levels, including Rab11-adaptor

493   binding, adaptor activities, adaptor-motor binding, dynein recruitment/binding to

494   microtubules and motor activity itself, and these regulations often involve protein

495   phosphorylation (Dillman and Pfister, 1994; Vaughan et al., 2002; Horgan et al., 2010;

496   Otani et al., 2011; Fu and Holzbaur, 2013; Moughamian et al., 2013; Wang et al.,

497   2019). It would be of interest to determine whether apical constriction regulates

498   Rab11 vesicle transport by inducing alterations in the phosphorylation status of

499   proteins mediating this transport. Finally, apical constriction may bias the direction of

500   transport by generating a "sink" that retains the vesicles at the apical side. For

501   example, the F-actin meshwork enriched at the apical cortex during apical

502   constriction could serve as scaffolds to entrap the Rab11 vesicles or as tracks for

503   vesicle dissemination at the apical domain, thereby inhibiting the reverse transport of

504   vesicles.

505

506   Our results suggest a function of Rab11 vesicles in facilitating apical constriction after

507   myosin II activation. Apical enrichment of Rab11 vesicles has also been observed in

508   several other apical constriction mediated processes, including gastrulation and neural

509   tube formation in *Xenopus* and salivary gland invagination in *Drosophila* (Ossipova

510   et al., 2014, 2015; Le and Chung, 2021). Inhibition or mistargeting of Rab11 during

26

511 these processes results in impaired apical myosin II accumulation and defects in

512 apical constriction, demonstrating the important function of Rab11 in mediating

513 apical myosin II activation. In our study, while disrupting the "early" function of

514 Rab11 inhibited apical myosin II accumulation, disrupting the "late" function of

515 Rab11, which completely abolished apical Rab11 vesicles, did not affect the

516 accumulation of myosin II at the cell apex but instead impaired the spatial

517 organization of the actomyosin network. These findings, for the first time,

518 demonstrate that Rab11 has separate "early" and "late" functions in regulating apical

519 constriction during tissue folding.

520

521 In Rab11DN injected embryos, the appearance of frequent myosin breaks was

522 associated with severe fragmentation of apical AJs. We propose that the late function

523 of Rab11 in maintaining the integrity of the actomyosin network is attributed to its

524 role in regulating apical AJs. Breaks in the actomyosin network have also been

525 observed in other conditions where junctions are impaired (Sawyer et al., 2009;

526 Martin et al., 2010; Movie 10). In addition, disruption of microtubules during apical

527 constriction, which we show inhibited the apical-basal transport of Rab11 vesicles,

528 has been shown to cause dynamic separation of actomyosin fibers from AJs (Ko et al.,

529 2019). Notably, the elevated frequency of myosin breaks in Rab11DN-injected

530 embryos was most prominent at late stages of apical constriction as tension increases.

531 Furthermore, these breaks mainly occurred along anterior-posterior direction, where

532   the tension is higher (Martin et al., 2010). These observations suggest that Rab11-

533   mediated reinforcement of junction-actomyosin connections is important for the

534   supracellular actomyosin network to resist increased tissue tension as apical

535   constriction proceeds.

536

537   The mechanisms by which Rab11 reinforces AJs is unclear. We propose that this

538   function is mediated by apical Rab11 vesicles for the following reasons. Firstly, at the

539   apical side, Rab11 vesicles were enriched at AJs. And secondly, when these vesicles

540   were eliminated, AJs became more fragmented and the level of the junctional

541   component Jub was substantially reduced. Rab11 recycling endosomes have been

542   shown to regulate the delivery of E-cadherin to the AJs in a number of other cell and

543   tissue contexts (Lock and Stow, 2005; Langevin et al., 2005; Yashiro et al., 2014; Le

544   Droguen et al., 2015; Woichansky et al., 2016). However, we did not detect E-

545   cadherin-GFP signal on Rab11 vesicles during apical constriction. It is possible that

546   the signal was too weak to be detected by the method we used. Alternatively, these

547   vesicles may function to transport other junction components or regulators. Finally,

548   Rab11 vesicles may regulate the connection between AJ and actomyosin network by

549   delivering actin regulators to AJs, as dynamic actin turnover at AJs has been shown to

550   impact the detachment and reattachment of actomyosin network to AJs (Jodoin et al.,

551   2015). Future studies identifying the cargos of Rab11 vesicles during apical

552   constriction will be the key for understanding the molecular function of the vesicles.

Acknowledgments

Author Contributions

W.C. and B.H. designed the study. W.C. performed the experiments and analyzed the data. W.C. and B.H. wrote the manuscript.

Declaration of Interests

The authors declare no competing interests.

571 **STAR ★ Methods**

572

573 **Lead Contact and Materials Availability**

574 Further information and requests for resources and reagents should be directed to and

575 will be fulfilled by the Lead Contact, Bing He (bing.he@dartmouth.edu).

576

577 **Experimental Model and Subject Details**

578 *Drosophila melanogaster* flies were grown and maintained at 18°C and crosses were

579 raised and maintained at room temperature (21 – 23°C) unless otherwise mentioned.

580 All flies were raised on standard fly food. For embryo collection, flies with

581 corresponding genotype were used to set up cages and maintained at 18°C, and

582 embryos were collected from apple juice agar plate containing fresh yeast paste.

583

584 For most experiments, embryos expressing endogenously tagged YFP::Rab11 (Dunst

585 et al., 2015) (BDSC Stock#62549) were imaged to visualize Rab11 vesicles. We also

586 generated UAS-mCherry::Rab11 transgenic flies for dual-color imaging with other

587 GFP-tagged markers. For lines with UAS-driven transgenes or shRNA, we used

588 GAL4 driver lines carrying matα4-GAL-VP16 (denoted as "mat67" on the 2nd

589 chromosome and "mat15" on the 3rd chromosome) to drive maternal expression in

590 the embryo through either direct cross or recombination.

591

592   The following fly lines were generated for dual-color imaging of Rab11 with other

593   markers in this study:

594   – Sqh::mCherry; YFP::Rab11

595   – Gap43::mCherry/Cyo; YFP::Rab11

596   – mat67 mCherry::Rab11; mat15 GFP::Jupiter

597   – mat67 mCherry::Rab11; mat15 E-cadherin::GFP

598   – mat67 mCherry::Rab11;mat15 mCherry::P4M

599

600   Figure S1: To examine other organelle behavior during apical constriction, the

601   following lines were either directly used or first crossed to mat67; mat15 flies in order

602   to obtain embryos expressing the corresponding fluorescent marker:

603   – UAS-Arf79F::GFP (BDSC Stock#65850)

604   – UAS-KDEL::GFP (BDSC Stock#9898)

605   – UAS-YFP::Rab7 (BDSC Stock#23641)

606   – YFP::Rab5 (BDSC Stock#62543)

607   – YFP::Rab8 (BDSC Stock#62546)

608

609   Figure 2C: To knock down myosin II, female flies of a TRiP *zipper*; YFP::Rab11

610   stock generated from a TRiP *zipper* RNAi line (BDSC Stock#37480) were crossed to

611   male flies from stock mat67 Sqh::mCherry; mat15 YFP::Rab11 to obtain F1 TRiP

612   *zipper*/mat67 Sqh::mCherry; YFP::Rab11/mat15 YFP::Rab11 flies, and embryos from

31

613   these F1 flies were collected for imaging.

614

615   Figure 2D: To generate ventralized embryos, *Spn27A1*/Cyo; Sqh::mCherry

616   YFP::Rab11/TM3 was crossed to Df(2L)BSC7/Cyo; Sqh::mCherry YFP::Rab11/TM3

617   to obtain *Spn27A1*/ Df(2L)BSC7; Sqh::mCherry YFP::Rab11 flies, and embryos from

618   these flies were collected for imaging.

619

620   Figure 2E: The fly stock used for temperature shift experiment is shi^{ts}/ shi^{ts};

621   Sqh::mCherry; YFP::Rab11.

622

623   Figure 5 and S3: Female flies from stock CRY2::mCherry::Rho1DN

624   YFP::Rab11/TM6C; CIBNpm/FM7 were crossed to male flies from stock mat67

625   Sqh::mCherry; mat15 YFP::Rab11 to generate mat67 Sqh::mCherry/+;

626   CRY2::mCherry::Rho1DN YFP::Rab11/mat15 YFP::Rab11; CIBNpm/+ flies, and

627   embryos from these flies were collected for imaging.

628

629   Figure 6: Sqh::mCherry E-cadherin::GFP was used for Rab11DN injection

630   experiment for examining adherens junction phenotype and quantifying apical area

631   change. Sqh::mCherry mat67; mat15 UAS-Jub::GFP was used for figure 6G.

632

633   Figure S3: To visualize the localization of constitutively active Rab11, UAS-

32

634   YFP::Rab11Q70L (BDSC Stock#9791) was crossed to mat67; mat15 males, and

635   embryos from F1 females were used for imaging.

636

637   Movie 10: A TRiP *canoe* RNAi line (BDSC Stock#38194) was used for *canoe*

638   knockdown. Female flies from the TRiP *canoe* stock were crossed to male flies from

639   stock mat67 Sqh::mCherry; mat15 E-cad::GFP to obtain F1 TRiP *canoe*/mat67

640   Sqh::mCherry; +/mat15 E-cad::GFP flies, and embryos from these F1 flies were

641   collected for imaging.

642

643   **Method details**

644   **Molecular cloning and generation of transgenic fly lines**

645   To make construct for in vitro expression of recombinant dominant negative Rab11

646   (S25N) protein, dominant negative Rab11 coding sequence was PCR amplified from

647   genomic DNA of UAS-YFPRab11DN (BDSC Stock#9792) and inserted into pGEX-

648   6p-1 vector (a gift from the Griffin lab, Dartmouth College) using BamHI and XhoI

649   restriction sites.

650

651   To make constructs for transgenic fly lines, mCherry-P4M double strand DNA was

652   synthesized in vitro (Integrated DNA Technologies) and inserted into a fly

653   transformation vector (pTiger, courtesy of S. Ferguson, State University of New York

654   at Fredonia, Fredonia, NY, USA) using NotI and NheI restriction site to generate the

33

655   pTiger-mCherry-P4M plasmid.

656

657   To make pTiger-mCherry-Rab11 construct, wild type Rab11 coding sequence was

658   PCR amplified from genomic DNA of UAS-YFP::Rab11 (BDSC Stock# 9790) and

659   cloned into pTiger-mCherry-P4M construct using SpeI and NheI restriction sites to

660   replace the P4M sequence.

661

662   The resulting pTiger-mCherry-P4M and pTiger-mCherry-Rab11 constructs were sent

663   to BestGene, Inc., for integration into either attP2 or attP40 site using the phiC31

664   integrase system (Groth et al., 2004).

665

666   **Live imaging and optogenetics**

667   Embryos were dechorionated in 3% bleach, rinsed with water 12 times and mounted

668   in water in a 35 mm MatTek glass-bottom dish (MatTek Corporation). Unless

669   otherwise mentioned, all images were obtained using a Nikon inverted spinning disk

670   confocal microscope equipped with the perfect focus system and Andor W1 dual

671   camera, dual spinning disk module. An CFI Plan Apo Lambda 60×/1.40 WD 0.13 mm

672   Oil Objective Lens objective was used for imaging at room temperature. YFP and

673   GFP tagged proteins were imaged with a 488-nm laser and mCherry tagged proteins

674   were imaged with a 561-nm laser. Images in Figure 1A, S1A and B were obtained

675   using an upright Olympus FV-MPERS multiphoton microscope equipped with the

34

676   InSight Deep Laser System with an Olympus 25X/1.05 water dipping objective

677   (XLPLN25×WMP2). Images in Figure 1D, 2A, 2D, S2, S3 were obtained using a

678   Zeiss Axio Observer laser scanning confocal microscope (LSM 880).

679

680   For optogenetic experiments, flies were kept in the dark and live sample preparation

681   was performed under red light. Embryos were first imaged with 561-nm laser to

682   visualize myosin II signal to determine the developmental stage of the embryo. Once

683   the embryo reached the desired stage, two-color imaging with both 488-nm and 561-

684   nm lasers were carried out, where the 488-nm laser was used for both optogenetic

685   stimulation and YFP-Rab11 visualization.

686

687   For the temperature shift experiment with shi^{ts} mutants, a Zeiss Axio Observer laser

688   scanning confocal microscope (LSM 880) with an incubation chamber was used.

689   Embryos subjected to restrictive temperature were prepared at room temperature and

690   then transferred to an incubation chamber, which was preheated to 32°C. A 40X/1.3

691   numerical aperture oil-immersion objective, and 488-nm argon laser and 561-nm laser

692   were used for imaging.

693

694   **Rab11 dominant negative protein expression and purification**

695   pGEX-6p-1-Rab11DN plasmid was transformed into E.coli (BL21(DE3), New

696   England BioLabs). An empty vector with only GST coding sequence was also

35

697   transformed as control. After IPTG induction, bacteria were resuspended in 32 mL

698   lysis buffer (50 mM Tris pH7.5, 150 mM NaCl, 0.1% Triton X-100, 1 mM PMSF, 1

699   mM DTT) and lysed with 0.25 mg/mL lysozyme incubation on ice for 2 h followed

700   by sonication (6 rounds of 10 pulses every 1 minute). GST and GST-Rab11DN were

701   purified from the supernatant with Glutathione Sepharose 4B GST-tagged protein

702   purification resin (GE17-0756-01, Sigma-Aldrich) using batch method. Eluted protein

703   was dialyzed using slide-A-Lyzer dialysis cassettes (Cat#66380, Thermo Scientific)

704   with 50 mM Tris buffer (pH8.0) and further concentrated to a final concentration of

705   ~200 μM with Amicon Ultra-0.5mL centrifugal filters (Cat#UFC501024, Millipore

706   Sigma).

707

708   **On-stage drug / protein injection**

709   Embryos at cellularization stage were prepared as previously described, then mounted

710   ventral side down on a 50 x 25 mm glass coverslip pre-covered with a thin layer of

711   glue. Embryos were dried for 10-15 minutes in a desiccator. Embryos were then

712   covered with halocarbon oil (halocarbon 700/halocarbon 27 = 3:1). A homemade

713   injection device mounted next to the spinning disk confocal microscope was used for

714   on-stage injection. Embryos were injected laterally into the ventral part of the

715   embryo. 50 mM Y-27632 (Enzo Life Sciences) and 25 mg/mL colchicine (Sigma-

716   Aldrich) were used. For Rab11DN injection, Triton X-100 was added to a final

717   concentration of 0.1% to prevent the solution from clogging the needle. For dynein

718   and GST antibody injection, commercial monoclonal antibodies against cytoplasmic

719   dynein intermediate chain (Cat#sc-13524, Santa Cruz Biotechnology) and monoclonal

720   antibody against GST (Cat#sc-138, Santa Cruz Biotechnology) were first

721   concentrated to 2 mg/mL with Amicon Ultra-0.5 mL centrifugal filters before

722   injection (Cat#UFC501024, Millipore Sigma).

723

724   **Quantification and Statistical Analysis**

725   **Image processing and analysis**

726   All images were processed using ImageJ (NIH) and MATLAB (MathWorks). For the

727   following figures, due to laser power fluctuation and the extent of photobleaching

728   with different imaging duration, the contrast was adjusted to make the cytoplasmic

729   signal comparable: Figure 2A, 2B (Rab11), 2C (myosin II), 2D (myosin II and

730   Rab11), S2(myosin II and Rab11), 4C (Rab11), 4H (myosin II and Rab11), 5E, 5F,

731   6A.

732

733   For vesicle tracking (Figure 3C-F, J, K), a 13.8 μm x 6.9 μm region of interest

734   including approximately one constricting cell at 50% egg length was selected, and

735   Rab11 vesicles were manually marked frame by frame for each trajectory using a

736   multi-point tool in ImageJ. The x-y coordinates of individual vesicles over time were

737   then exported. A MATLAB script was written to reconstruct the trajectories based on

738   the coordinate information. The direction of each trajectory was defined by the

739 relative translocation of the vesicle along apical basal axis between trackable start and

740 end positions. All trajectories were grouped into two categories based on their

741 direction (apical or basal) for further analysis of parameters, including trajectory

742 count, average velocity, trajectory length and trajectory duration.

743

744 For quantification of vesicle density in 2D (Figure 4D-F), 3 separate ROIs covering

745 most of the constriction region were selected, with each ROI enclosing a relatively

746 flat piece of tissue surface (based on the apical myosin II signal). For each ROI, a Z

747 position near the apical surface where most vesicles were accumulated was selected

748 for quantification. Vesicles were detected using the Find Maxima function in ImageJ

749 in combination with manual correction to ensure accuracy of the counting. For vesicle

750 counting in 3D (Figure 4D-F), the FIJI plugin 3D Maxima Finder was used and the

751 noise tolerance parameter was determined based on average intensity of the entire

752 image stack (Ollion et al., 2013).

753

754 The colocalization between Rab11-mCherry and E-cadherin-GFP was quantified in

755 embryos at the stage of early ventral furrow formation (Figure 5B-D). For each

756 embryo, 5 non-neighboring constricting cells were manually segmented using a multi-

757 point tool to mark the vertices of the cell outline. A MATLAB script was written to

758 import the coordinates of these vertices to create the cell outline. For each cell outline,

759 a series of closely spaced and evenly distributed sampling points were generated

760 along the outline. For each sampling point, E-cadherin-GFP signal intensity on that

761 single pixel   was extracted as the junction signal, and average Rab11-mCherry signal

762 intensity within a radius of 5 pixels (~0.54 μm) was calculated as Rab11 signal for the

763 same point. For each cell, a scatter plot of E-cadherin intensity over Rab11 intensity

764 for all the sampling points was generated, and a correlation coefficient was calculated.

765 A similar analysis was performed between P4M-GFP and Rab11-mCherry as a

766 control.

767

768 For myosin II intensity quantification (Figure 6B), 100-pixel by 100-pixel ROIs (10.8

769 μm X 10.8 μm) were taken from the apical myosin II domain. Average intensity R

770 was measured inside the ROI on that plane, and background noise at the same plane

771 (R_{bg}) was measured as the mean intensity of a random ROI outside the embryo. To

772 assess cytoplasmic myosin intensity (C), we used the same ROI position but at a

773 slightly deeper Z below the apical myosin network, the background noise at that plane

774 (C_{bg}) was measured as described above. The normalized myosin II intensity I = (R-

775 R_{bg}) / (C-C_{bg}). Embryos at ~6 – 7 min after the onset of gastrulation were used for

776 quantification.

777

778 For quantification of myosin breaks (Figure 6J, K), a maximum projection over 3 – 5

779 μm thick Z stacks that include all apical myosin II signal was generated. A ~100-sec

780 time window starting from the time point when the myosin II domain at the ventral

39

781   surface exhibits a relatively clear domain boundary (~6 – 7 min after the onset of

782   gastrulation) was selected to count the number of myosin break events. At the site

783   where myosin break occurs, the myosin fiber usually snaps and the two ends rapidly

784   retract, which creates a clear gap between neighboring myosin clusters.

785

786   To quantify the rate of apical constriction based on the movement of apical myosin II

787   structures (Figure 6D-G), kymographs were generated from the same dataset of the

788   above-mentioned 100-sec myosin movies. For each embryo, a series of myosin

789   kymographs were generated by average projection over every 30 pixels (3.2 μm)

790   along anterior posterior axis. Bandpass filter in ImageJ were used to remove noise. A

791   MATLAB script was used for automatic segmentation of individual myosin traces and

792   fitting with lines. Rate of myosin II moving towards ventral midline was extracted by

793   calculating the slope of each myosin trace. Velocity of myosin II at ventral midline

794   was subtracted to correct for the drift of ventral midline itself. The rate of myosin

795   movement was then plotted against the distance of the corresponding myosin structure

796   to ventral midline at the time when tracing started.

797

798   To quantify the rate of apical constriction from E-cadherin-GFP movies (Figure S4A,

799   B), images at 6 – 7 μm below the apical surface were used to measure the cell area

800   change over time. A group of constricting cells at the ventral most region of the

801   embryo were outlined frame by frame using multi-point tool in ImageJ. The area of

40

802   the same cell group over time was then calculated and plotted using MATLAB.

803

804   To analyze the distribution of cell area in the same embryo at 2 min, 5 min and 8 min

805   after onset of gastrulation (Figure S4C-E), individual constricting cell was segmented

806   using Embryo Development Geometry Explorer (EDGE), a MATLAB-based software

807   (Gelbart et al., 2012). Individual cell area was then calculated, and the distribution

808   histogram of cell area was plotted . Cell anisotropy was calculated based on the same

809   segmented cell dataset (Figure S4F). Two orthogonal (anteroposterior and

810   mediolateral) lines passing the centroid of the cell were drawn across the segmented

811   cell, and the cell anisotropy was calculated as the ratio between the anteroposterior

812   intercept by the cell boundary and the mediolateral intercept.

813

814   **Statistics**

815   Statistical comparisons were performed using two tailed one-sample t test or two-tailed

816   Student's t tests. Sample sizes can be found in figure legends. p values were calculated

817   using MATLAB ttest (Two tailed one-sample t test) and ttest2 function (Two tailed

818   Student's t test).

819 **Key Resources Table**

REAGENT or RESOURCE	SOURCE	IDENTIFIER
Chemicals and Antibodies		
Y-27632	Enzo Life Sciences	270-333-M005
Colchicine	Sigma-Aldrich	C9754-500MG
Dynein IC1/2 mouse monoclonal antibody	Santa Cruz Biotechnology	Sc-13524
GST(B-14) mouse monoclonal antibody	Santa Cruz Biotechnology	Sc-138
Experimental Models: Organisms/Strains		
D.melanogaster: YFP-Rab11	Bloomington Stock Center	BDSC:62549
D.melanogaster: UAS-mCherry-Rab11	This study	N/A
D.melanogaster: matαTub-Gal4VP16 67 (mat67)	Hunter and Wieschaus, 2000 (Wieschaus Lab)	N/A
D.melanogaster: matαTub-Gal4VP16 15 (mat15)	Hunter and Wieschaus, 2000 (Wieschaus Lab)	N/A
D.melanogaster: Sqh-mCherry	Martin et al 2009	N/A

	(Wieschaus Lab)	
D.melanogaster: UAS-GFP-Jupiter	Bloomington Stock Center	BL6836
D.melanogaster: E-cadherin-GFP	Oda, H. & Tsukita, S. J. Cell Sci. 114, 493–501 (2001).	N/A
D.melanogaster: UAS-mCherry-P4M	This study	N/A
D.melanogaster: UAS-Arf79F-GFP	Bloomington Stock Center	BDSC: 65850
D.melanogaster: UAS-KDEL-GFP	Bloomington Stock Center	BDSC: 9898
D.melanogaster: UAS-YFP-Rab7	Bloomington Stock Center	BDSC: 23641
D.melanogaster: YFP-Rab5	Bloomington Stock Center	BDSC: 62543
D.melanogaster: YFP-Rab8	Bloomington Stock Center	BDSC: 62546
D.melanogaster: UASp-YFP-Rab11Q70L	Bloomington Stock Center	BDSC: 9791
D.melanogaster: UASp-YFP-	Bloomington Stock	BDSC: 9792

Rab11S25N	Center	
D.melanogaster: UASp-YFP-Rab11	Bloomington Stock Center	BDSC: 9790
D.melanogaster: Jub-GFP/TM2	Bloomington Stock Center	BDSC: 56086
D.melanogaster: UASp-CRY2-mCherry-Rho1DN	Guo et al In preparation	N/A
D.melanogaster: UASp-CIBNpm	Guglielmi et al., 2015	N/A
D.melanogaster: TRiP Zipper	Bloomington Stock Center	BDSC: 37480
D.melanogaster: shi^{ts}	Bloomington Stock Center	BDSC: 7068
D.melanogaster: S$pn27A1$/Cyo	http://flybase.org/reports/FBrf0151901.html	N/A
D.melanogaster: Df(2L)BSC7/Cyo	Bloomington Stock Center	BDSC: 6374
D.melanogaster: TRiP cno	Bloomington Stock Center	BDSC: 38194
Oligonucleotides		

Forward primer for making mCherry-P4M construct: AAAAGCGGCCGCATGGTGAGCAAGGGCGAG		N/A
Reverse primer for making mCherry-P4M construct: TTTTGCTAGCTTATTTTATCTTAATGGTTTGTCTTTCTTG		N/A
Forward primer for making mCherry-Rab11 construct: AAAAACTAGTATGGGTGCAAGAGAAGACGA		N/A
Reverse primer for making mCherry-Rab11 construct: aaaaGCTAGCTCACTGACAGCACTGTTTGCG		N/A
Forward primer for pGEX6p-1-Rab11DN cloning: AAAAGGATCCATGGGTGCAAGAGAAGACGA		N/A
Reverse primer for pGEX6p-1-		N/A

	46	
Rab11DN cloning: AAAACTCGAGTCACTGACA GCACTGTTTGCG		
Software and Algorithms		
Matlab	MathWorks	https://www.mathworks.com/?s_tid=gn_logo; RRID:SCR_001622
FIJI	ImageJ	http://fiji.sc; RRID:SCR_002285
Embryo Development Geometry Explorer (EDGE)	Gelbart et al., 2012	https://github.com/mgelbart/embryo-development-geometry-explorer
Inkscape		https://inkscape.org/

820

821 *Reference:*

822 Ahmed, W.W., and Saif, T.A. (2014). Active transport of vesicles in neurons is
823 modulated by mechanical tension. Scientific Reports *4*, 4481.

824 Ahmed, W.W., Li, T.C., Rubakhin, S.S., Chiba, A., Sweedler, J.V., and Saif, T.A.
825 (2012). Mechanical Tension Modulates Local and Global Vesicle Dynamics in
826 Neurons. Cel. Mol. Bioeng. *5*, 155–164.

827 Amano, M., Ito, M., Kimura, K., Fukata, Y., Chihara, K., Nakano, T., Matsuura, Y., and
828 Kaibuchi, K. (1996). Phosphorylation and Activation of Myosin by Rho-associated
829 Kinase (Rho-kinase)*. Journal of Biological Chemistry *271*, 20246–20249.

830 Benli, M., Döring, F., Robinson, D.G., Yang, X., and Gallwitz, D. (1996). Two GTPase
831 isoforms, Ypt31p and Ypt32p, are essential for Golgi function in yeast. The EMBO
832 Journal *15*, 6460–6475.

833 van der Bliek, A.M., and Meyerowrtz, E.M. (1991). Dynamin-like protein encoded by
834 the Drosophila shibire gene associated with vesicular traffic. Nature *351*, 411–414.

835 Boycott, H.E., Barbier, C.S.M., Eichel, C.A., Costa, K.D., Martins, R.P., Louault, F.,
836 Dilanian, G., Coulombe, A., Hatem, S.N., and Balse, E. (2013). Shear stress triggers
837 insertion of voltage-gated potassium channels from intracellular compartments in atrial
838 myocytes. Proceedings of the National Academy of Sciences *110*, E3955–E3964.

839 Chanet, S., Miller, C.J., Vaishnav, E.D., Ermentrout, B., Davidson, L.A., and Martin,
840 A.C. (2017). Actomyosin meshwork mechanosensing enables tissue shape to orient cell
841 force. Nature Communications *8*, 15014.

842 Chen, W., Feng, Y., Chen, D., and Wandinger-Ness, A. (1998). Rab11 Is Required for
843 Trans-Golgi Network–to–Plasma Membrane Transport and a Preferential Target for
844 GDP Dissociation Inhibitor. MBoC *9*, 3241–3257.

845 Collinet, C., and Lecuit, T. (2021). Programmed and self-organized flow of information
846 during morphogenesis. Nature Reviews Molecular Cell Biology 1–21.

847 Coravos, J.S., and Martin, A.C. (2016). Apical Sarcomere-like Actomyosin Contracts
848 Nonmuscle Drosophila Epithelial Cells. Developmental Cell *39*, 346–358.

849 Dawes-Hoang, R.E., Parmar, K.M., Christiansen, A.E., Phelps, C.B., Brand, A.H., and
850 Wieschaus, E.F. (2005). folded gastrulation, cell shape change and the control of
851 myosin localization. Development *132*, 4165–4178.

852 Dunst, S., Kazimiers, T., von Zadow, F., Jambor, H., Sagner, A., Brankatschk, B.,
853 Mahmoud, A., Spannl, S., Tomancak, P., Eaton, S., et al. (2015). Endogenously Tagged

854 Rab Proteins: A Resource to Study Membrane Trafficking in Drosophila.
855 Developmental Cell *33*, 351–365.

856 Esteves da Silva, M., Adrian, M., Schätzle, P., Lipka, J., Watanabe, T., Cho, S., Futai,
857 K., Wierenga, C.J., Kapitein, L.C., and Hoogenraad, C.C. (2015). Positioning of AMPA
858 Receptor-Containing Endosomes Regulates Synapse Architecture. Cell Reports *13*,
859 933–943.

860 Fletcher, D.A., and Mullins, R.D. (2010). Cell mechanics and the cytoskeleton. Nature
861 *463*, 485–492.

862 Gauthier, N.C., Fardin, M.A., Roca-Cusachs, P., and Sheetz, M.P. (2011). Temporary
863 increase in plasma membrane tension coordinates the activation of exocytosis and
864 contraction during cell spreading. Proceedings of the National Academy of Sciences
865 *108*, 14467–14472.

866 Gelbart, M.A., He, B., Martin, A.C., Thiberge, S.Y., Wieschaus, E.F., and Kaschube,
867 M. (2012). Volume conservation principle involved in cell lengthening and nucleus
868 movement during tissue morphogenesis. Proceedings of the National Academy of
869 Sciences *109*, 19298–19303.

870 Gheisari, E., Aakhte, M., and Müller, H.-A.J. (2020). Gastrulation in Drosophila
871 melanogaster: Genetic control, cellular basis and biomechanics. Mechanisms of
872 Development *163*, 103629.

873 Gilmour, D., Rembold, M., and Leptin, M. (2017). From morphogen to morphogenesis
874 and back. Nature *541*, 311–320.

875 Groth, A.C., Fish, M., Nusse, R., and Calos, M.P. (2004). Construction of Transgenic
876 Drosophila by Using the Site-Specific Integrase From Phage φC31. Genetics *166*,
877 1775–1782.

878 Grünfelder, C.G., Engstler, M., Weise, F., Schwarz, H., Stierhof, Y.-D., Morgan, G.W.,
879 Field, M.C., and Overath, P. (2003). Endocytosis of a Glycosylphosphatidylinositol-
880 anchored Protein via Clathrin-coated Vesicles, Sorting by Default in Endosomes, and
881 Exocytosis via RAB11-positive Carriers. MBoC *14*, 2029–2040.

882 Guglielmi, G., Barry, J.D., Huber, W., and De Renzis, S. (2015). An Optogenetic
883 Method to Modulate Cell Contractility during Tissue Morphogenesis. Developmental
884 Cell *35*, 646–660.

885 He, B., Doubrovinski, K., Polyakov, O., and Wieschaus, E. (2014). Apical constriction
886 drives tissue-scale hydrodynamic flow to mediate cell elongation. Nature *508*, 392.

887 Horgan, C.P., Hanscom, S.R., Jolly, R.S., Futter, C.E., and McCaffrey, M.W. (2010).

888 Rab11-FIP3 links the Rab11 GTPase and cytoplasmic dynein to mediate transport to
889 the endosomal-recycling compartment. J Cell Sci *123*, 181–191.

890 Jedd, G., Mulholland, J., and Segev, N. (1997). Two New Ypt GTPases Are Required
891 for Exit From the Yeast trans-Golgi Compartment. J Cell Biol *137*, 563–580.

892 Jodoin, J.N., Coravos, J.S., Chanet, S., Vasquez, C.G., Tworoger, M., Kingston, E.R.,
893 Perkins, L.A., Perrimon, N., and Martin, A.C. (2015). Stable Force Balance between
894 Epithelial Cells Arises from F-Actin Turnover. Developmental Cell *35*, 685–697.

895 Karpova, N., Bobinnec, Y., Fouix, S., Huitorel, P., and Debec, A. (2006). Jupiter, a new
896 Drosophila protein associated with microtubules. Cell Motility *63*, 301–312.

897 Kennedy, M.J., Hughes, R.M., Peteya, L.A., Schwartz, J.W., Ehlers, M.D., and Tucker,
898 C.L. (2010). Rapid blue-light–mediated induction of protein interactions in living cells.
899 Nature Methods *7*, 973–975.

900 Khandelwal, P., Prakasam, H.S., Clayton, D.R., Ruiz, W.G., Gallo, L.I., van Roekel,
901 D., Lukianov, S., Peränen, J., Goldenring, J.R., and Apodaca, G. (2013). A Rab11a-
902 Rab8a-Myo5B network promotes stretch-regulated exocytosis in bladder umbrella
903 cells. MBoC *24*, 1007–1019.

904 Kimura, K., Ito, M., Amano, M., Chihara, K., Fukata, Y., Nakafuku, M., Yamamori, B.,
905 Feng, J., Nakano, T., Okawa, K., et al. (1996). Regulation of Myosin Phosphatase by
906 Rho and Rho-Associated Kinase (Rho-Kinase). Science *273*, 245–248.

907 Kirby, T.J., and Lammerding, J. (2016). Stretch to express. Nature Materials *15*, 1227–
908 1229.

909 Ko, C.S., Tserunyan, V., and Martin, A.C. (2019). Microtubules promote intercellular
910 contractile force transmission during tissue folding. J Cell Biol *218*, 2726–2742.

911 Langevin, J., Morgan, M.J., Rossé, C., Racine, V., Sibarita, J.-B., Aresta, S., Murthy,
912 M., Schwarz, T., Camonis, J., and Bellaïche, Y. (2005). Drosophila Exocyst
913 Components Sec5, Sec6, and Sec15 Regulate DE-Cadherin Trafficking from Recycling
914 Endosomes to the Plasma Membrane. Developmental Cell *9*, 365–376.

915 Lapierre, L.A., Kumar, R., Hales, C.M., Navarre, J., Bhartur, S.G., Burnette, J.O.,
916 Provance, D.W., Mercer, J.A., Bähler, M., and Goldenring, J.R. (2001). Myosin Vb Is
917 Associated with Plasma Membrane Recycling Systems. MBoC *12*, 1843–1857.

918 Le, T.P., and Chung, S. (2021). Regulation of apical constriction via microtubule- and
919 Rab11-dependent apical transport during tissue invagination. BioRxiv 827378.

920 Le Droguen, P.-M., Claret, S., Guichet, A., and Brodu, V. (2015). Microtubule-

921 dependent apical restriction of recycling endosomes sustains adherens junctions during
922 morphogenesis of the Drosophila tracheal system. Development *142*, 363–374.

923 Lee, J.-Y., and Harland, R.M. (2010). Endocytosis Is Required for Efficient Apical
924 Constriction during Xenopus Gastrulation. Current Biology *20*, 253–258.

925 Leptin, M., and Grunewald, B. (1990). Cell shape changes during gastrulation in
926 Drosophila. Development *110*, 73–84.

927 Ligoxygakis, P., Roth, S., and Reichhart, J.-M. (2003). A Serpin Regulates Dorsal-
928 Ventral Axis Formation in the Drosophila Embryo. Current Biology *13*, 2097–2102.

929 Lipatova, Z., Tokarev, A.A., Jin, Y., Mulholland, J., Weisman, L.S., and Segev, N.
930 (2008). Direct Interaction between a Myosin V Motor and the Rab GTPases Ypt31/32
931 Is Required for Polarized Secretion. MBoC *19*, 4177–4187.

932 Lock, J.G., and Stow, J.L. (2005). Rab11 in Recycling Endosomes Regulates the
933 Sorting and Basolateral Transport of E-Cadherin. MBoC *16*, 1744–1755.

934 Martin, A.C. (2020). The Physical Mechanisms of Drosophila Gastrulation: Mesoderm
935 and Endoderm Invagination. Genetics *214*, 543–560.

936 Martin, A.C., and Goldstein, B. (2014). Apical constriction: themes and variations on a
937 cellular mechanism driving morphogenesis. Development *141*, 1987–1998.

938 Martin, A.C., Kaschube, M., and Wieschaus, E.F. (2009). Pulsed contractions of an
939 actin–myosin network drive apical constriction. Nature *457*, 495–499.

940 Martin, A.C., Gelbart, M., Fernandez-Gonzalez, R., Kaschube, M., and Wieschaus, E.F.
941 (2010). Integration of contractile forces during tissue invagination. The Journal of Cell
942 Biology *188*, 735–749.

943 Mason, F.M., Tworoger, M., and Martin, A.C. (2013). Apical domain polarization
944 localizes actin–myosin activity to drive ratchet-like apical constriction. Nature Cell
945 Biology *15*, 926–936.

946 Mateus, A.M., Gorfinkiel, N., Schamberg, S., and Martinez Arias, A. (2011). Endocytic
947 and Recycling Endosomes Modulate Cell Shape Changes and Tissue Behaviour during
948 Morphogenesis in Drosophila. PLoS One *6*.

949 Mazumdar, A., and Mazumdar, M. (2002). How one becomes many: Blastoderm
950 cellularization in Drosophila melanogaster. BioEssays *24*, 1012–1022.

951 Mei, K., and Guo, W. (2018). The exocyst complex. Current Biology *28*, R922–R925.

952 Miao, H., Vanderleest, T.E., Jewett, C.E., Loerke, D., and Blankenship, J.T. (2019). Cell

953 ratcheting through the Sbf RabGEF directs force balancing and stepped apical
954 constriction. J Cell Biol jcb.201905082.

955 Narumiya, S., Ishizaki, T., and Ufhata, M. (2000). Use and properties of ROCK-specific
956 inhibitor Y-27632. In Methods in Enzymology, W.E. Balch, C.J. Der, and A. Hall, eds.
957 (Academic Press), pp. 273–284.

958 Nikolaidou, K.K., and Barrett, K. (2004). A Rho GTPase Signaling Pathway Is Used
959 Reiteratively in Epithelial Folding and Potentially Selects the Outcome of Rho
960 Activation. Current Biology *14*, 1822–1826.

961 Ollion, J., Cochennec, J., Loll, F., Escudé, C., and Boudier, T. (2013). TANGO: a
962 generic tool for high-throughput 3D image analysis for studying nuclear organization.
963 Bioinformatics *29*, 1840–1841.

964 Ossipova, O., Kim, K., Lake, B.B., Itoh, K., Ioannou, A., and Sokol, S.Y. (2014). Role
965 of Rab11 in planar cell polarity and apical constriction during vertebrate neural tube
966 closure. Nature Communications *5*, 3734.

967 Ossipova, O., Chuykin, I., Chu, C.-W., and Sokol, S.Y. (2015). Vangl2 cooperates with
968 Rab11 and Myosin V to regulate apical constriction during vertebrate gastrulation.
969 Development *142*, 99–107.

970 Oztan, A., Silvis, M., Weisz, O.A., Bradbury, N.A., Hsu, S.-C., Goldenring, J.R.,
971 Yeaman, C., and Apodaca, G. (2007). Exocyst requirement for endocytic traffic directed
972 toward the apical and basolateral poles of polarized MDCK cells. Mol Biol Cell *18*,
973 3978–3992.

974 Pelissier, A., Chauvin, J.-P., and Lecuit, T. (2003). Trafficking through Rab11
975 Endosomes Is Required for Cellularization during Drosophila Embryogenesis. Current
976 Biology *13*, 1848–1857.

977 Razzell, W., Bustillo, M.E., and Zallen, J.A. (2018). The force-sensitive protein Ajuba
978 regulates cell adhesion during epithelial morphogenesis. Journal of Cell Biology *217*,
979 3715–3730.

980 Riggs, B., Rothwell, W., Mische, S., Hickson, G.R.X., Matheson, J., Hays, T.S., Gould,
981 G.W., and Sullivan, W. (2003). Actin cytoskeleton remodeling during early Drosophila
982 furrow formation requires recycling endosomal components Nuclear-fallout and
983 Rab11. Journal of Cell Biology *163*, 143–154.

984 Sawyer, J.K., Harris, N.J., Slep, K.C., Gaul, U., and Peifer, M. (2009). The Drosophila
985 afadin homologue Canoe regulates linkage of the actin cytoskeleton to adherens
986 junctions during apical constriction. The Journal of Cell Biology *186*, 57–73.

Schonteich, E., Wilson, G.M., Burden, J., Hopkins, C.R., Anderson, K., Goldenring, J.R., and Prekeris, R. (2008). The Rip11/Rab11-FIP5 and kinesin II complex regulates endocytic protein recycling. Journal of Cell Science *121*, 3824–3833.

Schroeder, H.W., Mitchell, C., Shuman, H., Holzbaur, E.L.F., and Goldman, Y.E. (2010). Motor Number Controls Cargo Switching at Actin-Microtubule Intersections In Vitro. Current Biology *20*, 687–696.

Schroeder, H.W., Hendricks, A.G., Ikeda, K., Shuman, H., Rodionov, V., Ikebe, M., Goldman, Y.E., and Holzbaur, E.L.F. (2012). Force-Dependent Detachment of Kinesin-2 Biases Track Switching at Cytoskeletal Filament Intersections. Biophysical Journal *103*, 48–58.

Schuh, M. (2011). An actin-dependent mechanism for long-range vesicle transport. Nature Cell Biology *13*, 1431–1436.

Shillcock, J.C., and Lipowsky, R. (2005). Tension-induced fusion of bilayer membranes and vesicles. Nature Materials *4*, 225–228.

Siechen, S., Yang, S., Chiba, A., and Saif, T. (2009). Mechanical tension contributes to clustering of neurotransmitter vesicles at presynaptic terminals. Proceedings of the National Academy of Sciences *106*, 12611–12616.

Staykova, M., Holmes, D.P., Read, C., and Stone, H.A. (2011). Mechanics of surface area regulation in cells examined with confined lipid membranes. PNAS *108*, 9084–9088.

Sun, S., and Irvine, K.D. (2016). Cellular Organization and Cytoskeletal Regulation of the Hippo Signaling Network. Trends in Cell Biology *26*, 694–704.

Sweeton, D., Parks, S., Costa, M., and Wieschaus, E. (1991). Gastrulation in Drosophila: the formation of the ventral furrow and posterior midgut invaginations. Development *112*, 775–789.

Takahashi, S., Kubo, K., Waguri, S., Yabashi, A., Shin, H.-W., Katoh, Y., and Nakayama, K. (2012). Rab11 regulates exocytosis of recycling vesicles at the plasma membrane. J Cell Sci *125*, 4049–4057.

Tiwari, A.K., and Roy, J.K. (2008). Rab11 is essential for fertility in Drosophila. Cell Biology International *32*, 1158–1168.

Uhler, C., and Shivashankar, G.V. (2017). Regulation of genome organization and gene expression by nuclear mechanotransduction. Nature Reviews Molecular Cell Biology *18*, 717–727.

1020 Ullrich, O., Reinsch, S., Urbé, S., Zerial, M., and Parton, R.G. (1996). Rab11 regulates
1021 recycling through the pericentriolar recycling endosome. J Cell Biol *135*, 913–924.

1022 Vasquez, C.G., Tworoger, M., and Martin, A.C. (2014). Dynamic myosin
1023 phosphorylation regulates contractile pulses and tissue integrity during epithelial
1024 morphogenesis. J Cell Biol *206*, 435–450.

1025 Wang, Z., Edwards, J.G., Riley, N., Provance, D.W., Karcher, R., Li, X., Davison, I.G.,
1026 Ikebe, M., Mercer, J.A., Kauer, J.A., et al. (2008). Myosin Vb Mobilizes Recycling
1027 Endosomes and AMPA Receptors for Postsynaptic Plasticity. Cell *135*, 535–548.

1028 Welz, T., Wellbourne-Wood, J., and Kerkhoff, E. (2014). Orchestration of cell surface
1029 proteins by Rab11. Trends in Cell Biology *24*, 407–415.

1030 Weng, M., and Wieschaus, E. (2016). Myosin-dependent remodeling of adherens
1031 junctions protects junctions from Snail-dependent disassembly. J Cell Biol *212*, 219–
1032 229.

1033 Winter, C.G., Wang, B., Ballew, A., Royou, A., Karess, R., Axelrod, J.D., and Luo, L.
1034 (2001). Drosophila Rho-Associated Kinase (Drok) Links Frizzled-Mediated Planar
1035 Cell Polarity Signaling to the Actin Cytoskeleton. Cell *105*, 81–91.

1036 Woichansky, I., Beretta, C.A., Berns, N., and Riechmann, V. (2016). Three mechanisms
1037 control E-cadherin localization to the zonula adherens. Nature Communications *7*,
1038 10834.

1039 Wu, S., Mehta, S.Q., Pichaud, F., Bellen, H.J., and Quiocho, F.A. (2005). Sec15
1040 interacts with Rab11 via a novel domain and affects Rab11 localization in vivo. Nature
1041 Structural & Molecular Biology *12*, 879–885.

1042 Wu, X.-S., Elias, S., Liu, H., Heureaux, J., Wen, P.J., Liu, A.P., Kozlov, M.M., and Wu,
1043 L.-G. (2017). Membrane Tension Inhibits Rapid and Slow Endocytosis in Secretory
1044 Cells. Biophysical Journal *113*, 2406–2414.

1045 Yashiro, H., Loza, A.J., Skeath, J.B., and Longmore, G.D. (2014). Rho1 regulates
1046 adherens junction remodeling by promoting recycling endosome formation through
1047 activation of myosin II. MBoC *25*, 2956–2969.

1048 Yi, J.Y., Ori-McKenney, K.M., McKenney, R.J., Vershinin, M., Gross, S.P., and Vallee,
1049 R.B. (2011). High-resolution imaging reveals indirect coordination of opposite motors
1050 and a role for LIS1 in high-load axonal transport. Journal of Cell Biology *195*, 193–
1051 201.

1052 Zhang, X.-M., Ellis, S., Sriratana, A., Mitchell, C.A., and Rowe, T. (2004). Sec15 Is an
1053 Effector for the Rab11 GTPase in Mammalian Cells*. Journal of Biological Chemistry

1054   *279*, 43027–43034.

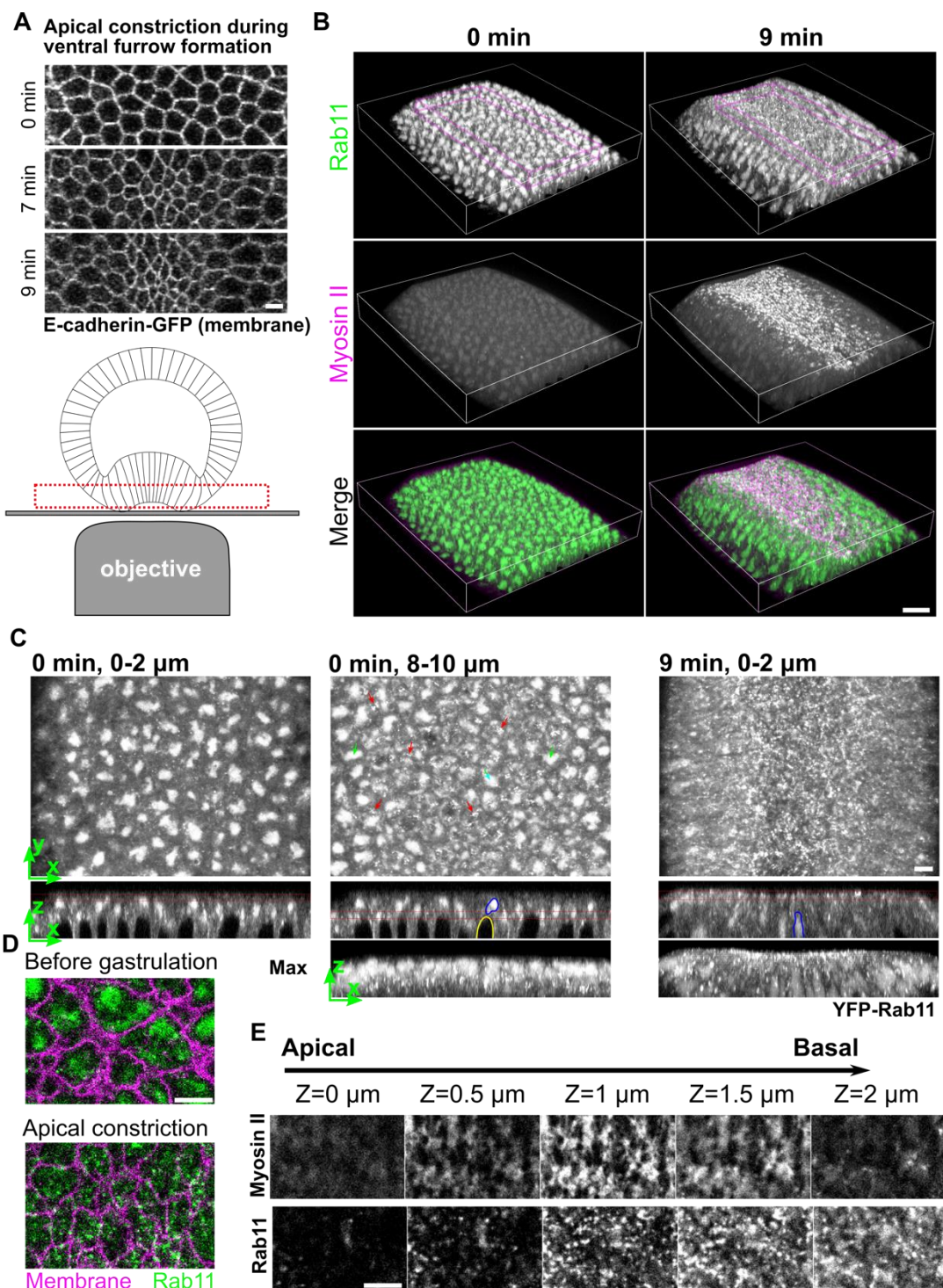1055 **Figure 1**

55

1057 **Figure 1. Rab11-positive vesicle-like structures accumulate apically in**

1058 **constricting cells during ventral furrow formation**

1059 (A) Apical constriction during ventral furrow formation. Scale bar, 10 μm. The

1060 bottom panel shows the imaging setup for acquiring the en face view of constricting

1061 cells.

1062 (B) 3-D reconstruction of the ventral part of an embryo expressing YFP-Rab11 and

1063 mCherry-Sqh during ventral furrow formation. Magenta box indicates the apical

1064 region of the constricting cells.

1065 (C) Rab11 compartments in an embryo at the onset (0 min) and 9 min into ventral

1066 furrow formation. Top panel, maximum projection over 2 μm depth from en face

1067 view; middle panel, a single slice cross section view; bottom panel, maximum

1068 projection of the cross section view. Red box indicates the Z position of the

1069 corresponding en face view. Red arrows: perinuclear Rab11 vesicles; green arrows

1070 and blue outlines: perinuclear Rab11 compartments; yellow outline: nucleus.

1071 (D) Zoom-in view of a small ROI in the ventral region of the embryo.

1072 (E) Montage showing YFP-Rab11 and mCherry-Sqh distribution over depth during

1073 apical constriction.

1074 All scale bars are 5 μm unless mentioned otherwise.
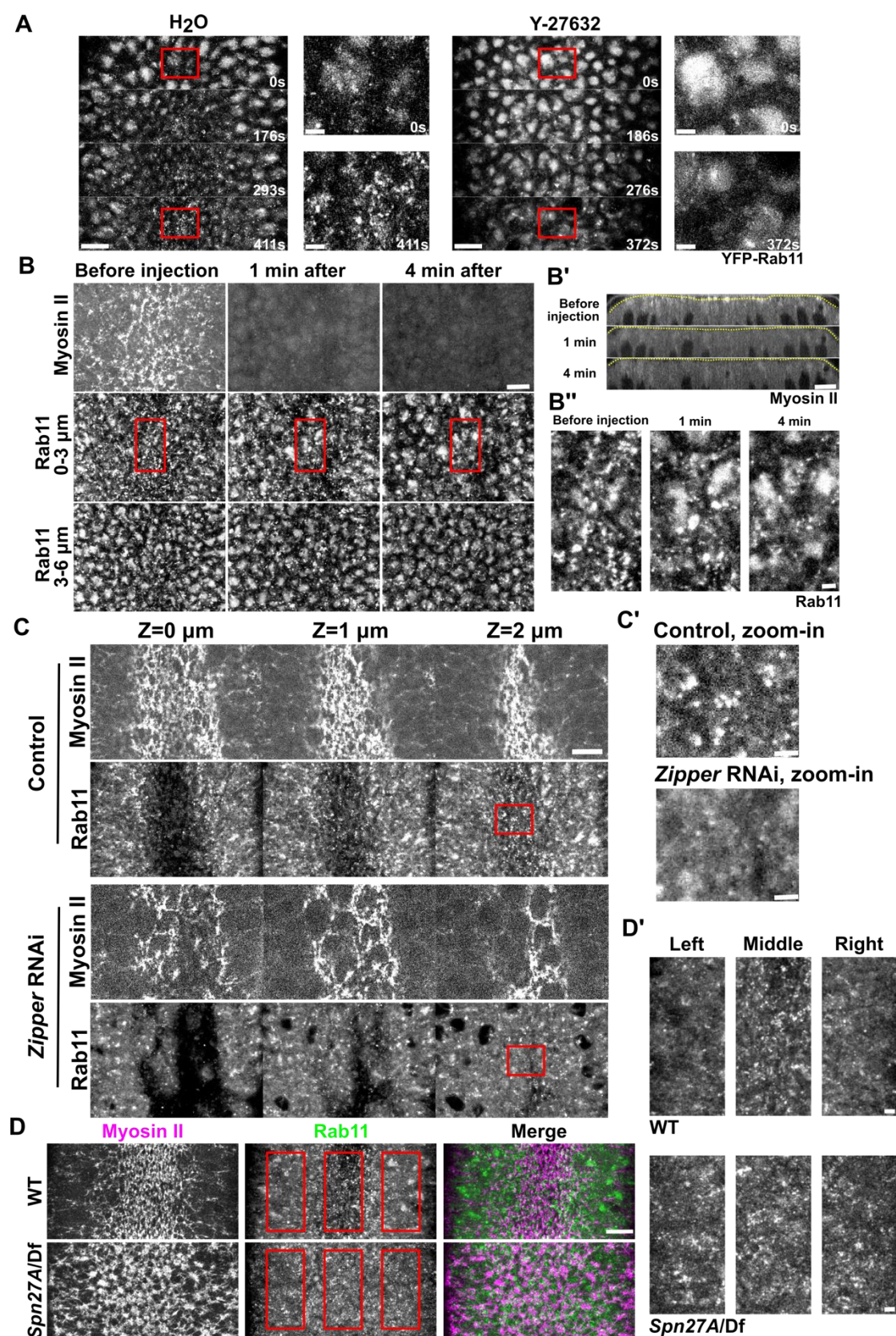
56

1075 **Figure 2**

1077 **Figure 2. Apical accumulation of Rab11 vesicles depends on apical constriction**

1078 (A) Inhibition of myosin II activation by Y-27632 injection at late cellularization

1079 prevents apical Rab11 vesicle accumulation. Shown are maximum projections of a ~3

1080 – 4 μm-stack below apical surface of the constriction domain (same for the other en

1081 face view images in this figure). The zoom-in view of regions marked by red boxes is

1082 shown to the right. 0 sec marks the onset of gastrulation. For Y-27632 injection: N = 4

1083 embryos; H_2O injection: N = 3 embryos. Contrasts were adjusted to make the

1084 background comparable.

1085 (B) Injection of Y-27632 during apical constriction causes rapid diminishing of apical

1086 Rab11 vesicles. N = 4 embryos. (B') Cross section view of the same embryo. Yellow

1087 dotted lines mark the apical outline highlighting tissue relaxation after drug injection.

1088 (B'') Zoom-in view of panel B.

1089 (C) Knockdown of myosin heavy chain Zipper inhibits apical accumulation of Rab11

1090 vesicle. N = 4 embryos for each genotype. (C') Zoom-in view of panel C.

1091 (D) *Spn27A*/Df mutant embryos exhibit ventralized phenotype with expanded domain

1092 of apical myosin II activation. The domain of apical Rab11 vesicle accumulation also

1093 expands accordingly (N = 3 embryos), as shown in (D') with zoom-in view of regions

1094 marked by red boxes in (D). Images were Gaussian filtered with a radius of 0.5 pixel.

1095 To improve the signal/noise, fewer apical z-slices were used to generate the projected

1096 images for the zoom-in view.

1097 All scale bars for zoom-in view , 2 μm; scale bars for the rest, 10 μm.

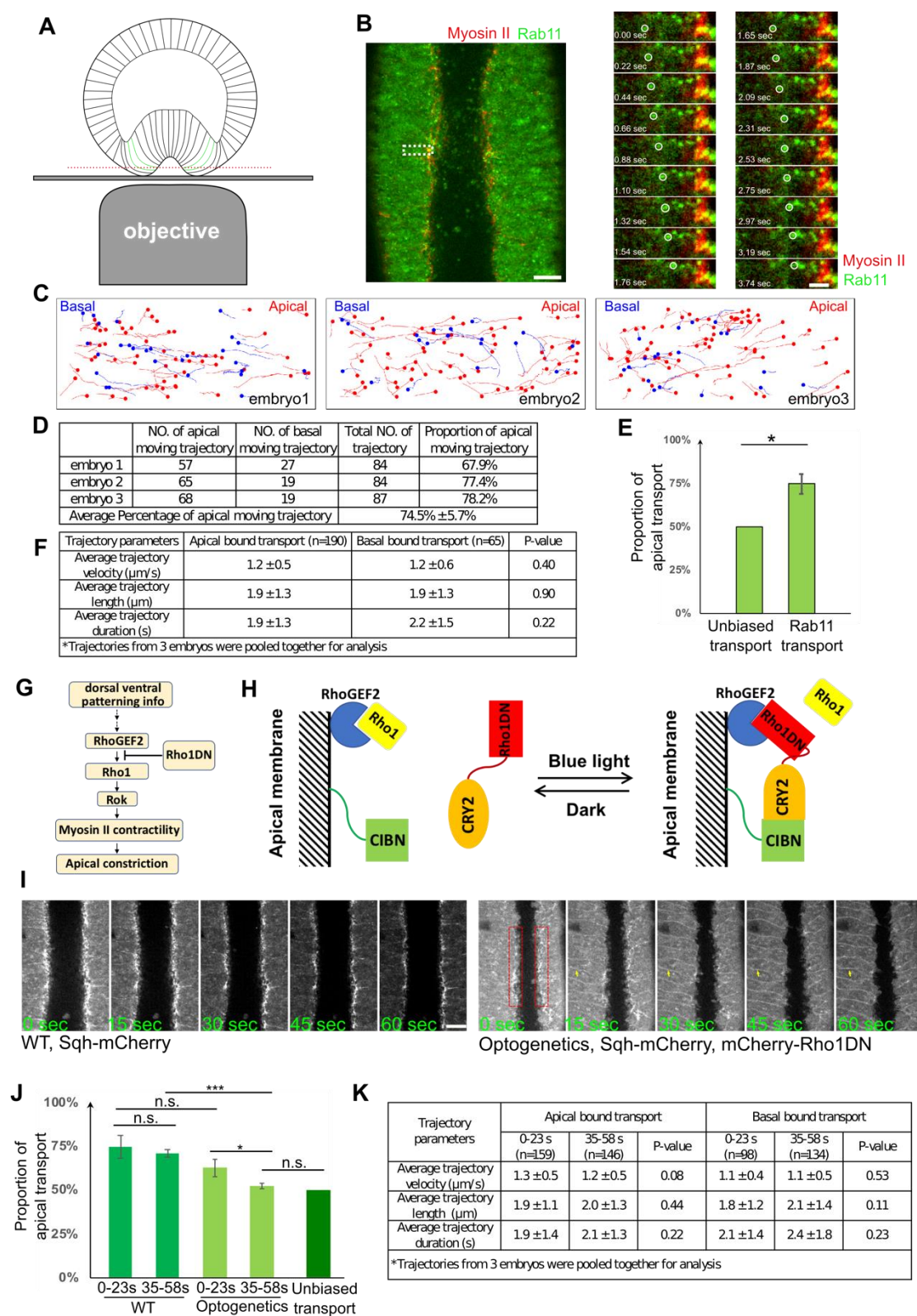58

1098 **Figure 3**

1099

1100 **Figure 3. Rab11 vesicles are transported apical-basally with a strong bias in the**

1101 **apical direction, which depends on activation of apical actomyosin contractility**

1102 (A) Imaging configuration to capture the movement of Rab11 vesicles along the

1103 apical-basal direction. Red dotted line indicates the imaging plane. Two constricting

1104 cells being imaged are marked in green.

1105 (B) Left: surface view of an embryo expressing Sqh-mCherry and YFP-Rab11. Scale

1106 bar, 10 μm. Right: zoom-in view of the marked region showing the movement of two

1107 Rab11 vesicles (white circles) towards apical myosin II. Scale bar, 2 μm.

1108 (C) Vesicle trajectories in 3 wildtype embryos in a ~35-sec time window. Red and

1109 blue mark apical- and basal-bound trajectories, respectively.

1110 (D) Counts of apically and basally oriented trajectories.

1111 (E) Rab11 vesicles exhibit directional bias towards the apical side. Two tailed one-

1112 sample t-test against 50%; N = 3 embryos. In all figures, Error bar stands for s.d.;

1113 ***: $p < 0.001$; **: $p < 0.01$; *: $p < 0.05$; n.s.: $p > 0.05$.

1114 (F) Comparison of average trajectory length, velocity and duration (mean ± s.d.)

1115 shows no significant difference between apically and basally directed transport. Two

1116 tailed Student's t-test; N = 3 embryos.

1117 (G) Upstream signaling pathway that activates myosin II driven apical constriction.

1118 (H) Diagram depicting optogenetic inhibition of myosin activation by Opto-Rho1DN.

1119 (I) Upon continuous blue light (488 nm) stimulation, Rho1DN is rapidly recruited to

1120 the plasma membrane (yellow arrows). Apical myosin II (red boxes) disappears from

60

1121   cell apices ~ 30 sec after stimulation. A wildtype embryo at similar stage of furrow

1122   formation is shown as a control. Scale bar, 10 μm.

1123   (J) The apical bias of the transport is abolished in less than one minute after

1124   stimulation in Opto-Rho1DN embryos (two tailed one-sample t-test against 50%).

1125   Two tailed Student's t test was used for all other statistical comparisons.

1126   (K) Average trajectory velocity, length and duration of apical and basal bound

1127   transports (mean ± s.d.). There is no significant difference between 0 – 23 sec and 35

1128   – 58 sec post stimulation time windows. Two tailed Student's t test; N = 3 embryos.
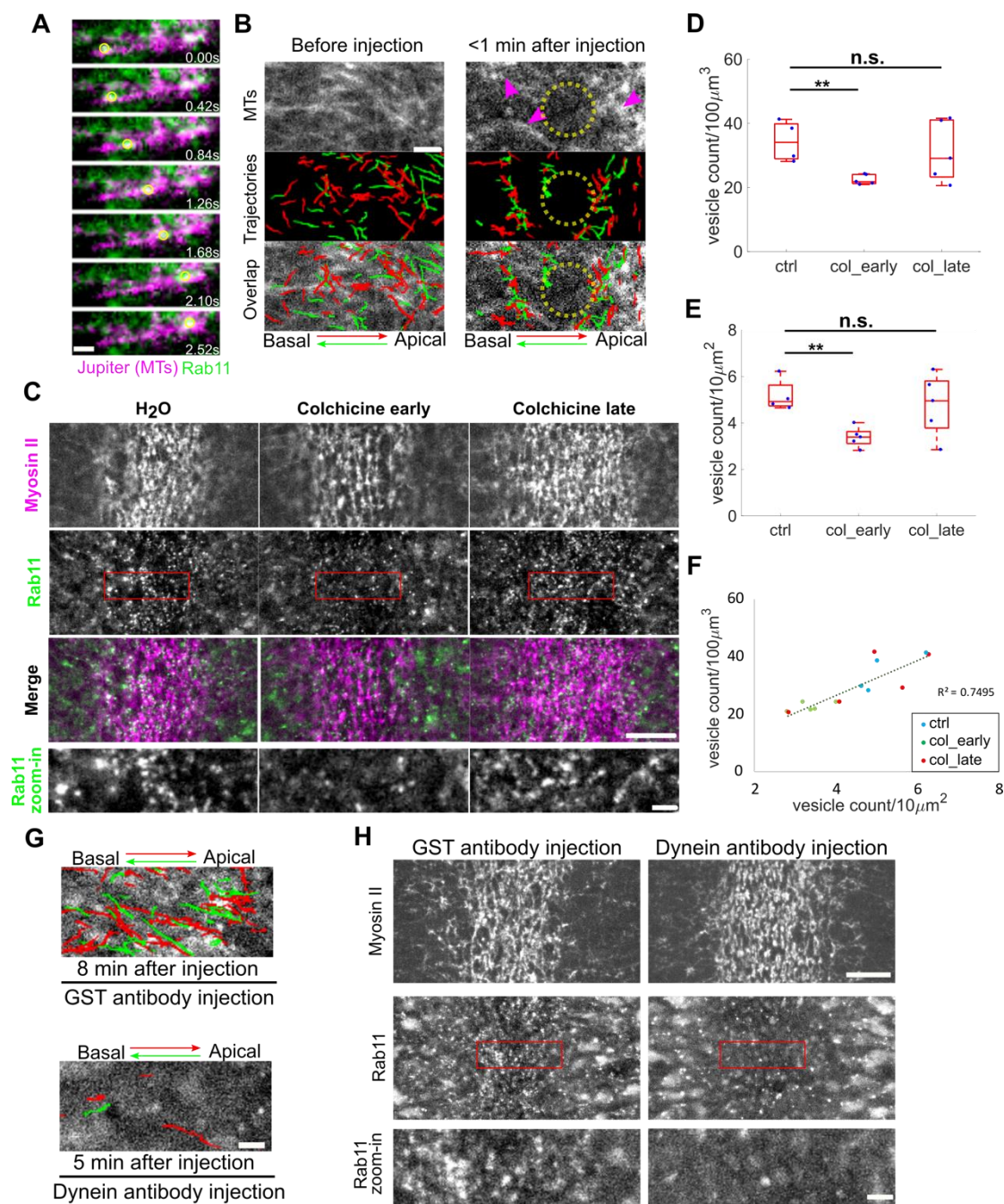
Figure 4

1129

62

1131 **Figure 4. Rab11 vesicle transport requires microtubules and dynein**

1132 (A) An example of Rab11 vesicle movement (yellow circle) along the microtubules

1133 (Jupiter-GFP). Scale bar, 1 μm.

1134 (B) Acute disruption of microtubules via on-stage injection of colchicine results in

1135 immediate inhibition of Rab11 vesicle transport. Images showing the same region

1136 before and one minute after injection. Magenta arrowheads indicate residual

1137 microtubules after colchicine injection. Yellow dotted circle marks a region where

1138 microtubules are completely disrupted. Scale bar, 2 μm.

1139 (C) En face view of the constricting domain shortly (< 2 min) after on-stage injection

1140 of water or colchicine. Injection of colchicine shortly before but not after the onset of

1141 gastrulation (N = 5 embryos for each condition) results in reduced Rab11 vesicle

1142 accumulation compared to water injected controls (N = 4 embryos). Scale bar, 10 μm.

1143 Zoom-in view of regions marked by red boxes are shown in the bottom. Scale bar, 2

1144 μm.

1145 (D-F) Quantification of Rab11 vesicle density after water or colchicine injection

1146 within a 3.5 μm-stack from apical surface (D) or in a single z plane near apical

1147 surface with the highest vesicle density (E). The two approaches are well consistent

1148 with each other (F).

1149 (G) On-stage injection of dynein antibody rapidly abolishes both apical and basal

1150 transport of Rab11 vesicles. Images showing the overlay between the Rab11 channel

1151 and the apically or basally targeted vesicle trajectories within a 20-sec time window at

1152   the indicated time after injection. N = 5 embryos for both DIC antibody and GST

1153   antibody injection. Scale bar, 2 μm.

1154   (H) En face view showing inhibition of apical accumulation of Rab11 vesicles upon

1155   on-stage injection of dynein antibody immediately before the onset of gastrulation. N

1156   = 5 and 6 embryos for GST antibody and dynein antibody injection, respectively.

1157   Scale bar, 10 μm. Zoom-in view of regions marked by red boxes are shown in the
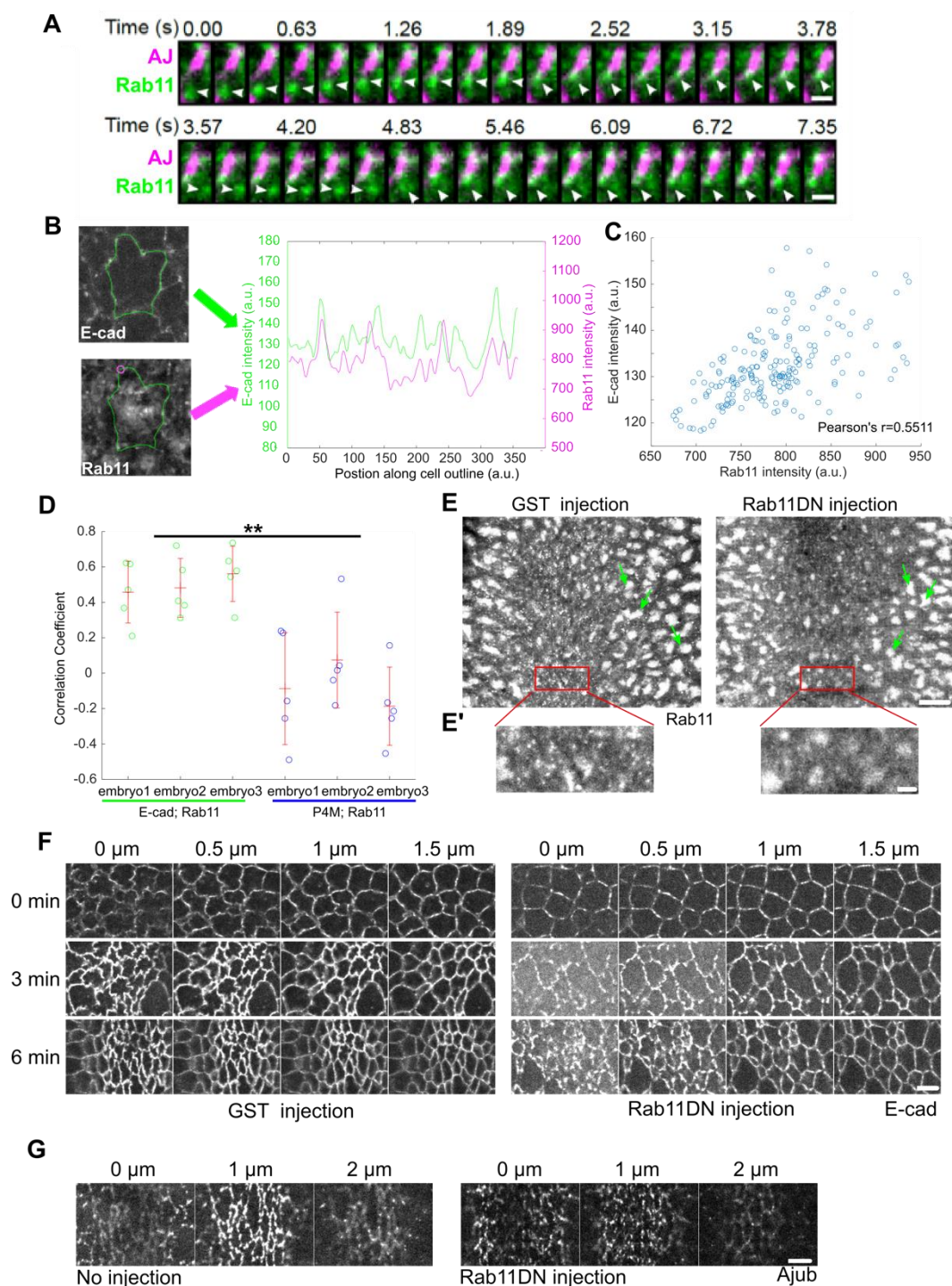
1158   bottom. Scale bar, 2 μm.

1159 **Figure 5**

1161 **Figure 5. Rab11 reinforces the apical adherens junctions (AJs) during ventral**

1162 **furrow formation**

1163 (A) Movie stills showing Rab11 vesicles moving towards an AJ spot. Scale bar, 1 μm.

1164 (B-D) Analysis of spatial correlation between Rab11 vesicles and AJs. (B) A

1165 constricting cell is outlined in green. Magenta marks the circle within which Rab11

1166 signal is measured. Right panel: the intensity profiles of E-cadherin and Rab11 along

1167 the indicated cell outline. (C) E-cadherin intensities for all points along the cell

1168 outline plotted against the corresponding Rab11 intensities. (D) Rab11 shows a

1169 significantly higher correlation with E-cadherin than with a general membrane marker

1170 P4M (N = 3 embryos for each genotype, 5 cells per embryo). Two tailed Student's t-

1171 test was used for statistical comparison. E-cad: E-cadherin.

1172 (E) Injection of dominant negative Rab11 (Rab11DN) eliminates apical Rab11

1173 vesicles but does not immediately affect the perinuclear Rab11 compartments (green

1174 arrows). Scale bar, 10 μm. (E') Zoom-in view of regions marked by red boxes. Scale

1175 bar, 2 μm.

1176 (F) Rab11DN injection affects the integrity of apical AJs in the constricting cells. 14

1177 out of 19 Rab11DN injected embryos show fragmented apical AJs while 8 of 8 GST

1178 injected embryos show relatively continuous AJs. Scale bar, 5 μm.

1179 (G) Upon Rab11DN injection, Ajub is more sparsely distributed at the apical AJs

1180 during apical constriction (N = 2 embryos for no injection control, N = 4 embryos for
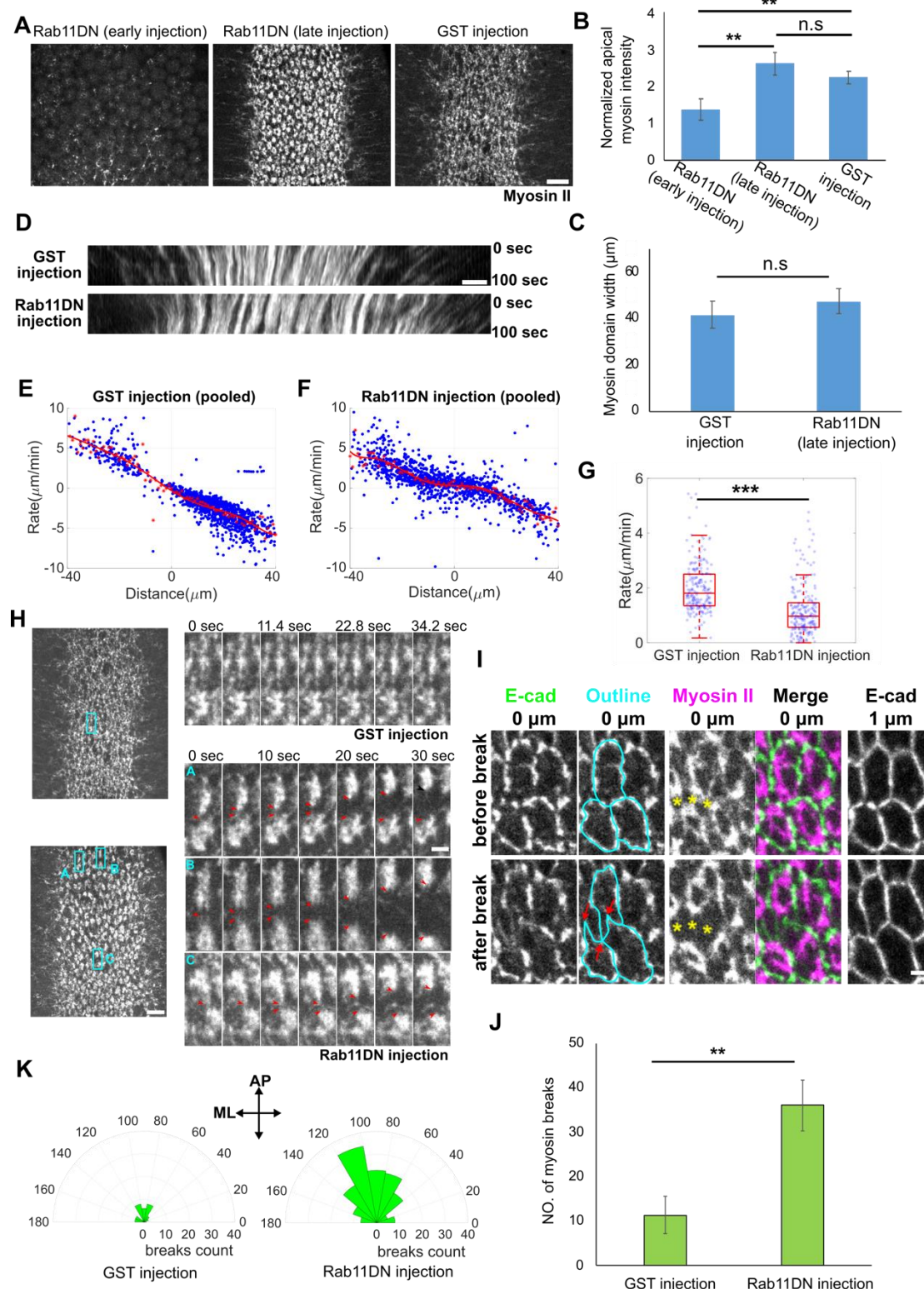
1181 Rab11DN injection). Scale bar, 5 μm.

66

1182 **Figure 6**

1183

1184 **Figure 6. Acute Inhibition of Rab11 results in defects in myosin II organization**

1185 **and apical constriction**

1186 (A-C) Stage-dependent effect of Rab11DN injection on apical myosin network. (A):

1187 Injection of Rab11DN at early cellularization (> 30 min before onset of gastrulation)

1188 impairs apical myosin II activation (N = 3 embryos), whereas injection around the

1189 onset of gastrulation does not affect myosin II activation but causes defects in apical

1190 myosin organization (N = 4 embryos). GST injection: N = 3 embryos. Scale bar, 10

1191 μm. (B, C): Quantification of apical myosin II intensity (B) and the width of myosin

1192 domain (C) at ~6-7 min after the onset of gastrulation. Two tailed Student's t-test was

1193 used for statistical comparison.

1194 (D) Example kymograph showing the movement of apical myosin II towards ventral

1195 midline at ~6-7 minutes into gastrulation. Only the late Rab11DN injected embryos

1196 were analyzed in (D) – (K). Scale bar, 5 μm.

1197 (E-G) Quantification of apical constriction rate in embryos injected with GST and

1198 Rab11DN. (E, F) Rate of myosin movement towards ventral midline is plotted against

1199 the distance of myosin structures from ventral midline at 0 sec. Red asterisks

1200 represent the average velocity at the corresponding position and the red curve is the

1201 polynomial fit of the average velocity along the medial-lateral direction. (G) The rate

1202 of movement for myosin structures located 10-15 μm away from the ventral midline

1203 is compared between GST and Rab11DN-injected embryos. Two tailed Student's t test

1204 was used for statistical comparison.

1205   (H-K) Injection of Rab11DN increases the frequency of myosin breaks during apical

1206   constriction. (H) Left, representative surface views of the supracellular myosin

1207   network in Rab11DN- and GST-injected embryos. Scale bar, 10 μm. Right, zoom-in

1208   view of the highlighted region (cyan boxes) showing myosin dynamics over time. Red

1209   arrowheads show separation of neighboring myosin structures after a break event

1210   happens. Scale bar, 2 μm. (I) Apical AJ is pulled inward (red arrows) when myosin

1211   break (yellow asterisks) occurs in the adjacent cell. Scale bar, 2 μm. (J) Quantification

1212   of the number of myosin breaks over a ~100-sec time window at ~6 – 7 min after

1213   apical constriction starts. Two tailed Student's t test was used for statistical

1214   comparison. (K) Quantification of myosin break orientation in GST- and Rab11DN-
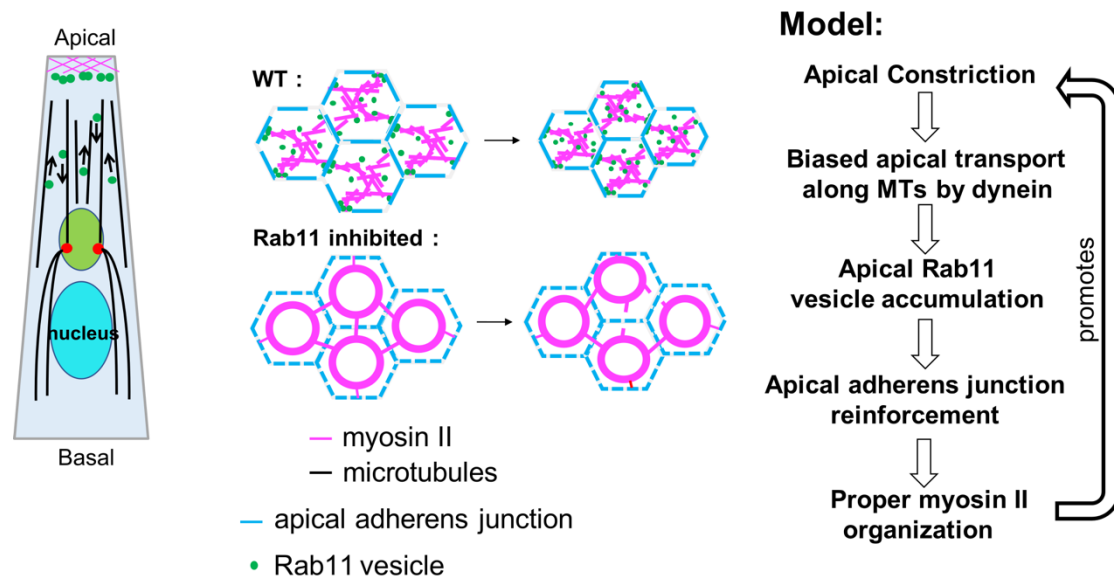
1215   injected embryos.

1216 **Figure 7**

1217

1218 **Figure 7. Schematics of proposed mechanosensitive feedback mechanism**

1219 During *Drosophila* ventral furrow formation, actomyosin contraction mediated apical

1220 constriction results in biased transport of Rab11 vesicles towards the apical surface,

1221 which leads to the apical accumulation of these vesicles. At the apical region, the

1222 Rab11 vesicles are targeted to apical AJs and function to reinforce the structural

1223 integrity of AJs. This mechanosensitive function of Rab11 is important for securing

1224 the anchoring sites for the contractile machinery at the cell-cell boundaries, which

1225 ensures proper organization of the supracellular actomyosin network and efficient

1226 apical constriction. When apical accumulation of Rab11 vesicles is inhibited, the

1227 constricting cells exhibit fragmented AJs, frequent myosin breaks and myosin ring

1228 formation, which reduces the rate of apical constriction.